KRISTI UUDEBERG

Optical Water Type Guided Approach to
Estimate Water Quality in Inland and
Coastal Waters

TARTU ÜLIKOOL · UNIVERSITAS TARTUENSIS · 1632

DISSERTATIONES PHYSICAE UNIVERSITATIS TARTUENSIS

**124**

# KRISTI UUDEBERG

Optical Water Type Guided Approach to Estimate Water Quality in Inland and Coastal Waters

This study was carried out at the Institute of Physics, University of Tartu, Estonia and Tartu Observatory, University of Tartu, Estonia.

The Dissertation was admitted on March 31, 2020 in partial fulfillment of the requirements for the degree of Doctor of Philosophy in physics and allowed for defense by the Council of the Institute of Physics, University of Tartu.

Supervisors:      Dr. Anu Noorma
                  Tartu Observatory, University of Tartu, Estonia

                  Dr. Kaire Toming
                  Estonian Marine Institute, University of Tartu, Estonia


Opponents:        Assoc. Prof. Susanne Kratzer
                  Stockholm University, Sweden

                  Prof. Kalev Sepp
                  Estonian University of Life Sciences, Estonia

The public defense will take place on June 2, 2020 at the University of Tartu.

# CONTENTS

# LIST OF ORIGINAL PUBLICATIONS

The present thesis is based on the following publications, which are referred to by Roman numerals in the text.

I. **Uudeberg, K.**; Ansko, I.; Põru, G.; Ansper, A.; Reinart, A. Using Optical Water Types to Monitor Changes in Optically Complex Inland and Coastal Waters. *Remote Sens.* 2019, *11*, 2297.

II. Soomets, T.; **Uudeberg, K.**; Jakovels, D.; Zagars, M.; Reinart, A.; Brauns, A.; Kutser, T. Comparison of Lake Optical Water Types Derived from Sentinel-2 and Sentinel-3. *Remote Sens.* 2019, *11*, 2883.

III. **Uudeberg, K**.; Aavaste, A.; Kõks, K.-L.; Ansper, A.; Uusõue, M.; Kangro, K.; Ansko, I.; Ligi, M.; Toming, K.; Reinart, A. Optical Water Type Guided Approach to Estimate Optical Water Quality Parameters. *Remote Sens*. 2020, *12*, 931.

IV. Soomets, T.; **Uudeberg, K.**; Jakovels, D.; Brauns, A.; Zagars, M.; Kutser, T. Validation and Comparison of Water Quality Products in Baltic Lakes Using Sentinel-2 MSI and Sentinel-3 OLCI Data. *Sensors* 2020, *20*, 742.

V. Alikas, K.; Ansko, I.; Vabson, V.; Ansper, A.; Kangro, K.; **Uudeberg, K.**; Ligi, M. Consistency of Radiometric Satellite Data over Lakes and Coastal Waters with Local Field Measurements. *Remote Sens.* 2020, *12*, 616.

VI. Reinart, A.; **Valdmets, K.** Variability of optical water types in Lake Peipsi. *Proceedings of the Estonian Academy of Sciences. Biology. Ecology* 2007, *56*, 33−46.

# Author's contribution

The publications on which this thesis is based are the results of collective work with contributions from all the authors.

The thesis author's contribution to articles **I** and **III** was the design of the study, preparation of data, performing most of the calculations, and writing the original draft of the manuscript. In **II** and **IV**, the author performed calculations and analyses related to optical water types and wrote the related text. In **V**, the author prepared initial data of *in situ* measurements and wrote the related text. In **VI**, the author prepared the data and had a major role in performing calculations and writing the original draft of the manuscript. The author participated in or organized collecting of the *in situ* data for articles **I**, **III**, **V**, and **VI**.

# ABBREVIATIONS AND ACRONYMS

| | |
|---|---|
| AC | Atmospheric correction |
| $a_{\mathrm{CDOM}}(442)$ | Absorption coefficient of CDOM at a wavelength of 442 nm, $\mathrm{m}^{-1}$ |
| ACOLITE | Atmospheric Correction for OLI 'lite' |
| ALTNN | Alternative Neural Net |
| AR | Algorithm reference |
| C2RCC | Case 2 Regional CoastColour |
| C2X | Case 2 Extreme |
| CDOM | Coloured dissolved organic matter |
| Chl-a | Chlorophyll-a, $\mathrm{mg \cdot m^{-3}}$ |
| $E_d(\lambda)$ | Spectral downwelling irradiance, $\mathrm{W \cdot m^{-2} \cdot nm^{-1}}$ |
| ESA | European Space Agency |
| GF/F | Glass fiber filters |
| IOP | Inherent optical properties |
| L2 | Level-2 |
| $L_{sky}(\lambda)$ | Spectral downwelling radiance from sky, $\mathrm{W \cdot m^{-2} \cdot nm^{-1} \cdot sr^{-1}}$ |
| $L_t(\lambda)$ | Spectral upwelling radiance form water surface, $\mathrm{W \cdot m^{-2} \cdot nm^{-1} \cdot sr^{-1}}$ |
| $L_u(\lambda)$ | Spectral upwelling radiance, $\mathrm{W \cdot m^{-2} \cdot nm^{-1} \cdot sr^{-1}}$ |
| MODIS | Moderate Resolution Imaging Spectroradiometer |
| MSAS | Modified spectral angle similarity |
| MSI | Multispectral Instrument |
| NIR | Near-infrared |
| OAT | One factor at a time |
| OLCI | Ocean and Land Colour Instrument |
| OSC | Optically significant constituent |
| OWT | Optical water type |
| PCA | Principal component analysis |
| POLYMER | POLYnomial-based algorithm applied previously to MERIS |
| $R(\lambda)$ | Spectral water-leaving reflectance |
| $R^2$ | Coefficient of determination |
| Ramses | Reflectance with 1 nm step resolution obtained from *in situ* measurements |
| $Rrs(\lambda)$ | Spectral remote sensing reflectance, $\mathrm{sr^{-1}}$ |
| SCS | Spectral correlation similarity |
| Sen2Cor | Sentinel-2 Correction |
| SPIM | Suspended particulate inorganic matter, $\mathrm{mg \cdot L^{-1}}$ |
| SPOM | Suspended particulate organic matter, $\mathrm{mg \cdot L^{-1}}$ |
| SRF | Spectral response function |
| TOA | Top of the atmosphere |
| TSM | Total suspended matter, $\mathrm{mg \cdot L^{-1}}$ |
| $w$ | Wind speed, $\mathrm{m \cdot s^{-1}}$ |
| ZSD | Secchi disk depth, m |
| $\lambda$ | Wavelength, nm |
| $\rho(w)$ | Air-sea interface reflection coefficient |

# 1. INTRODUCTION

Humans have long enjoyed living where the land and water meet; it is invigorating for the spirit. Water bodies are valued as sources of the water supply for domestic life and agricultural and industrial production, supporters of biodiversity, and providers of fishing and recreation opportunities. At the same time, the impact of human activities close to inland waters and coastal areas has increased, which has caused the deterioration of water bodies. Therefore, the state of a water body requires constant monitoring to assess the magnitude of the impact of human activity and to respond when needed. Traditional water monitoring programs are mainly based on *in situ* measurements; however, considering that water bodies are dynamic in nature, this method may not reflect the status of the whole water body. Also, the monitoring frequency is often not sufficient to capture changes or to detect them early enough to ameliorate water quality. Therefore, it is important to implement techniques that allow more operative monitoring of the aquatic environment.

Remote sensing offers effective ways to observe spatial and/or temporal variations in water quality, which is vital for the comprehensive assessment and management of water bodies [1]. In remote sensing, the physical characteristics of an area are monitored by measuring reflected and emitted radiation at a distance (e.g. using data from satellites, aircraft, towers, hand-held devices, etc.). Water quality can be estimated using a passive remote sensing technique by measuring sunlight that has been backscattered within the water in the visible and near-infrared (NIR) part of the spectrum. Sunlight altered by water masses is influenced by optically significant constituents (OSC) such as phytoplankton, coloured dissolved organic matter (CDOM), and total suspended matter (TSM). As inland and coastal waters contain greatly and independently varying amounts of different OSC, remote sensing of inland and coastal waters is very challenging [2].

Phytoplankton consists of single-celled, free-floating, photosynthetic organisms that form the base of the aquatic food web and are an important component of the carbon cycle, which has a major impact on water quality. Seasonal phytoplankton blooms are natural processes in the aquatic environment [3]. However, a rise in phytoplankton biomass may also be a sign of eutrophication, which indicates increased nutrient inputs [4,5], all of which, in turn, leads to drastic changes in the aquatic ecosystem (e.g., altered species composition, hypoxia, decreased water transparency, toxins, problems for fishes) [6,7]. Phytoplankton is primarily responsible for determining the optical properties of most oceanic waters. The photosynthetic phytoplankton pigment chlorophyll-a (Chl-a) is typically used as a proxy for phytoplankton biomass [8]. Chl-a strongly absorbs light in the blue and red regions of the visible spectrum [2]. Simple remote sensing algorithms for the retrieval of Chl-a are based on the ratios of reflectance, such as the blue-green ratio [9], which are empirically related to the Chl-a concentration. However, this is not often valid for optically

complex waters, where CDOM and TSM also affect the optical properties of water. Several studies have suggested the use of various combinations of NIR and red band combinations instead [10–12].

TSM is divided into suspended particulate organic matter (SPOM) and suspended particulate inorganic matter (SPIM). It is used as an indicator of physical forcing, for instance, wind-driven resuspension, land runoff, as well as dredging operations, which lead to much higher TSM concentrations in the area [13,14]. SPOM contains a mixture of planktonic organisms (e.g., phyto-plankton, bacterioplankton, etc.,) and non-living organic matter, and its optical properties are similar to those of CDOM [15]. The presence of terrigenous particles in the water often accounts for the bulk of SPIM. SPIM scatters light, whereas the scattering depends on the size and shape of the particles—particles < 1 μm scatter more strongly at shorter wavelengths, while in the case of larger particles, the wavelength dependence is weak [15,16]. This limits the accuracy of algorithms for estimating TSM. The use of red and/or NIR wavelengths is suggested to quantify the SPIM due to strong water absorption in the NIR wavelengths [17].

CDOM is an optically active fraction of dissolved organic matter [18]. It may have a local origin, for instance, from degradation of phytoplankton cells, or it may be advected from a distant source, for example, from organic-rich rivers. CDOM can be used as a proxy for assessing dissolved organic carbon dynamics, identifying organic pollution in agricultural and urban catchments, and detecting influences of anthropogenic activities (e.g., land-use change) [19]. Light absorption by CDOM is the strongest at shorter wavelengths of the spectrum. Absorbance increases exponentially with decreasing wavelengths and diminishes to near-zero in the red wavelength region [20]. Therefore, a wavelength of 440 nm is often used to estimate absorption by CDOM from remote sensing data [21,22].

The European Space Agency (ESA) has recently launched two Earth observation missions under the Copernicus program [23] that are suitable for monitoring the optical properties of inland and coastal waters. Sentinel-2 is a land monitoring mission that consists of two satellites (A and B, launched in 2015 and 2017, respectively) carrying the Multispectral Instrument (MSI), which offers high spatial resolution (10, 20, and 60 m) with 13 spectral bands [24]. MSI has opened new opportunities to investigate smaller water bodies [25] and different phenomena in more detail (e.g., filaments and eddies of biological activity) [26,27]. Sentinel-3 is an ocean and land mission that currently consists of two satellites (A and B, launched in 2016 and 2018, respectively). These carry the Ocean and Land Colour Instrument (OLCI), which has medium resolution (300 m) and 21 well-placed spectral bands to measure ocean colour over optically complex water bodies [28]. However, the rather low spatial resolution of OLCI allows the study of only about 1000 of the largest lakes on Earth [29] out of 117 million [30]. The free availability of Copernicus data with high spectral, spatial, and temporal resolution and with continuity plans for at

least a couple of decades has generated wide interest in the use of remote sensing capabilities to monitor water quality in inland and coastal waters.

Different approaches have been used to evaluate four main optical water quality parameters, such as concentrations of Chl-a and TSM, the absorption coefficient of CDOM at a wavelength of 442 nm ($a_{CDOM}$(442)), and Secchi disk depth (ZSD) from these sensors [31–34]. In the case of optically complex waters where optical properties are more diverse and can vary over short spans of time and space, standard remote sensing products often fail [31,35–37], which has led to the development of regionally specific algorithms [38]. However, regional algorithms also do not show consistency in terms of changes in their optical properties [31]. The possible solution could be to use remote sensing algorithms based on the classification of optical water types (OWTs).

Classification approaches are widely used in the remote sensing of land, and their popularity in water remote sensing has grown in recent years. For several decades, the Case 1 and Case 2 system by Morel and Prieur [39] was the most widely used classification for aquatic applications. Case 1 represents waters whose optical properties depend on phytoplankton, and Case 2 represents waters whose optical properties depend on independent sources of phyto-plankton, suspended sediments, and dissolved organic matter. Optically complex coastal and inland waters mainly belong to Case 2. However, these optically complex waters show great variability in optical properties, and their monitoring therefore requires a more detailed approach. Different approaches have been used to classify waters, such as using the diffuse attenuation coefficient of downwelling light [40], concentrations of OSC [41], inherent optical properties (IOP) [42], production of organic matter [43], water colour [44], and water-body health state [1]. However, due to the desire to move toward classifying waters based on satellite data, the most popular property used for classification has recently become reflectance spectra [45–52]. Reflectance spectra carry valuable information on the composition and amount of in-water constituents [53]. A variety of OWTs based on reflectance have been developed for ocean and marine waters [45,47,48,50,51]; the classification of OWTs for lakes has also recently come into focus [46,47,49,52]. However, it is difficult to find an already existing OWT classification applicable for the wide range of the boreal region's inland and coastal waters.

# 2. AIMS

The main aim of this thesis was to develop an approach to estimating the optical water quality parameters for boreal region inland and coastal waters, such as concentrations of Chl-a and TSM, $a_{\text{CDOM}}(442)$, and ZSD, from remote sensing data.
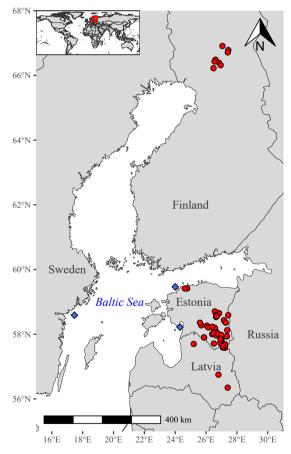
The specific aims of the thesis were:

- to investigate the impact of the measurement environment on the variability of *in situ* measurements of reflectance (**I**, **V**);
- to develop an OWT classification based on reflectance spectra that is applicable to data from OLCI and MSI (**I**, **VI**);
- to develop a solution to estimate optical water quality parameters from reflectance spectra with different spectral scales (**III**, **IV**);
- to compare the OWTs derived from OLCI and MSI to understand if the classifications of OWTs from both satellites are compatible (**II**);
- to find the most suitable OLCI and MSI processing steps to monitor temporal and spatial variability of water quality parameters (**I**, **II**, **III**, **IV**, **V**).

# 3. MATERIAL AND METHODS

## 3.1. Study Area

The study area includes Estonian, Finnish, and Latvian lakes and the Baltic Sea, all of which belong to the northern boreal region's inland and coastal waters (Figure 1). In addition, the Wadden Sea was included to expand the ranges of optical water properties.

*In situ* lake data was mainly collected from various Estonian lakes (42 lakes), ranging from small lakes, such as Lake Holstre (0.04 km2), to large lakes, such as Lake Peipus (3555 km$^2$), and from highly transparent lakes, such as Lake Nohipalo Valgjärv (ZSD 5 m), to very brown lakes, such as Nohipalo Mustjärv (ZSD 0.3 m). In addition, three lakes in Latvia and eight lakes in Finland were included in the study.



**Figure 1.** Location of water bodies included in the study. Inland waters are marked with red circles and coastal waters with blue diamonds. The location of the Wadden Sea is not shown on this map.

The Baltic Sea is a shallow, brackish intra-continental sea with limited water exchange with the North Sea. Three regions of the Baltic Sea were included in this study. Pärnu Bay is located on the west coast of Estonia, where the mean depth is 4.7 m (maximum 8 m) and the water is well mixed. Since Pärnu Bay is shallow, open to winds, and has a sandy, clayey, and muddy bottom, wind-derived resuspension can lead to quite high and quickly changing conditions of TSM concentrations. The second area is located in the Gulf of Finland region, where the mean depth is 37 m with a maximum of 123 m (Paldiski Deep), and where the water column is vertically stratified [16]. The area is prone to upwelling and downwelling events in the summer and autumn [54,55]. The third area is located in the Western Gotland Basin close to the coast of Sweden. Also located in the Western Gotland Basin is the Baltic Sea's deepest place, Landsort Deep (459 m), but in our measurement stations, the water depth was up to 30 m.

The Wadden Sea is a coastal sea between the North Sea and the mainland of the Netherlands, Germany, and Denmark. The area is shallow (maximum 12 m) and strongly affected by tides. The variation in water sources, such as tidal inlets from the North Sea and discharges from the rivers Rhine, Ems, Jade, Weser, and Elde, causes optical properties of water to change widely and quickly [56].

## 3.2. *In Situ* Dataset

The study was based on *in situ* measurements gathered from 53 Estonian (**I**, **III**, **IV**, **V**, **VI**), Finnish (**III**), and Latvian lakes (**IV**), from three coastal locations in the Baltic Sea (**I**, **III**, **V**), and from the Wadden Sea (**I**) during 2003–2006 and 2012–2019. The *in situ* dataset contained measurements of reflectance, concentrations of OSC (such as the concentration of Chl-a and TSM, and $a_{CDOM}(442)$), ZSD, and different environmental parameters (such as wind speed, wave height, cloudiness, and visibility of the sun). ZSDs were measured on the shadow side of the vessel using a white disk with a 30 cm diameter or a white disk with holes and a 20 cm diameter. The wind speed was measured with a handheld mechanical anemometer. The wave height, cloudiness, and visibility of the sun were estimated by visual inspection.

### 3.2.1. Measurements of Reflectance

Three reflectance measurement setups were used in this study according to specific goals: an above-water system with three TriOS-RAMSES hyperspectral radiometers (**I**, **III**, **V**), a profiling system with two TriOS-RAMSES hyper-spectral radiometers (**III**, **VI**), and an above-water system with a PSR-3500 spectrometer (**IV**).

For the first setup, the above-water system consisted of three TriOS-RAMSES hyperspectral radiometers: two radiance sensors measuring spectral

upwelling radiance ($L_t(\lambda)$) and spectral downwelling radiance ($L_{sky}(\lambda)$) in the same azimuthal plane, and one irradiance sensor measuring spectral down-welling irradiance ($E_d(\lambda)$). The radiance sensor's nadir/zenith angles of 40° were fixed in the frame. The measured spectral range was 350–900 nm. The recording interval was once per 10-second interval. The solar azimuth angle was kept between 90° and 180° and was adjusted manually during measure-ments. The calculation of spectral water-leaving reflectance ($R(\lambda)$) followed the protocol of REVAMP [57] and included the following steps. First, all measured radiance and irradiance spectra were linearly interpolated to a 1 nm step. Secondly, $R(\lambda)$ was calculated as

$$R(\lambda) = \pi \frac{L_t(\lambda) - \rho(w)L_{sky}(\lambda)}{E_d(\lambda)}, \tag{1}$$

where $\rho(w)$ is the air-sea interface reflection coefficient as function of wind speed ($w$, m·s$^{-1}$) and calculated as $\rho(w) = 0.0256 + 0.00039w + 0.000034w^2$ [57]. Finally, the median $R(\lambda)$ was calculated and used as the representative of the *in situ* measurement station. In Paper **V**, the calculation also included the stray light [58,59] and the NIR similarity corrections steps [60].

For the second setup, the profiling system consisted of two TriOS-RAMSES hyperspectral radiometers: one irradiance sensor measuring spectral down-welling irradiance ($E_d(\lambda)$) and one radiance sensor measuring spectral upwelling radiance ($L_u(\lambda)$). Measurements were made above the water, below the water surface, and at different depths in the water column. In this study, only above-water measurements were used. The measured spectral range was 350–900 nm. At every depth, five recordings were taken. The $R(\lambda)$ calculations included three steps. First, all measured spectra were linearly interpolated to a 1 nm step. Secondly, $R(\lambda)$ was calculated as

$$R(\lambda) = \pi \frac{L_u(\lambda)}{E_d(\lambda)}. \tag{2}$$

Finally, the median $R(\lambda)$ was calculated and used as the representative of the *in situ* measurement station.

For the third setup, the spectral remote sensing reflectance ($Rrs(\lambda)$) was measured above the surface (about 10 cm) using the hand-held spectrometer PSR-3500. The spectral range was 348–1000 nm, and a spectral sampling interval of approximately 1.5 nm. $Rrs(\lambda)$ was calculated as the ratio of radiance from water to radiance from a white standard Spectralon reference panel. Finally, the average $Rrs(\lambda)$ was calculated and used as representative of the *in situ* measurement station.

To understand the impact of the measurement environment on the variability of *in situ* measurements of $R(\lambda)$, logistic regression model analysis (**I**) and principal component analysis (PCA) (**V**) were performed with R software [61].

To study the implementation capacity of the OWTs (**I**, **III**, **IV**) or to validate satellite products (**IV**, **V**), the specific spectral response functions (SRFs) of the satellite sensor bands were used to convolve hyperspectral reflectance spectra representing the *in situ* measurement stations with certain satellite band data and calculated according to Paper **I**. The SRFs for the OLCI and MSI were taken from [62] and [63], respectively.

### 3.2.2. Measurements of Optical Water Quality Parameters

Water samples for measurements of the concentrations of OSC were collected from the water surface (up to 0.5 m depth) according to ISO 5667-3 [64] and analysed according to ISO 10260 [65]. For Chl-a, samples were filtered through Whatman GF/F filters, pigments were extracted with 5 ml of 96% ethanol and measured spectrophotometrically with a Hitachi U-3010 spectrophotometer, and calculated according to Jeffrey and Humphrey [66] (**I**, **III**, **IV**, **V**, **VI**), or the Thermo Helios γ spectrophotometer was used and the concentrations of Chl-a were calculated according to Lorenzen [67] (**III**). For TSM, samples were filtered through pre-washed, pre-ashed, and pre-weighed Whatman GF/F filters (**I**, **III**, **IV**, **V**, **VI**) or Millipore membrane filters with a pore size of 0.45 μm (**III**) and measured gravimetrically. For CDOM, samples were filtered through a filter with a pore size of 0.2 μm, measured in a 5 cm optical cuvette against distilled water with a Hitachi U-3010 spectrophotometer, and calculated according to Lindell *et al*. [68] (**I**, **III**, **IV**, **V**, **VI**).

### 3.3. Satellite Dataset

OLCI, onboard the Sentinel-3 satellite, full-resolution Level-1 (**I**, **II**, **III**, **IV**, **V**) and Level-2 (**I**, **V**) images and MSI, onboard the Sentinel-2, full-resolution Level-1 (**I**, **II**, **IV**) images acquired in 2016–2019 were used. OLCI Level-1 images were processed with the C2RCC [69] (**I**, **II**, **III**, **IV**, **V**), ALTNN [70] (**I**, **V**), and POLYMER [71] (**V**) atmospheric correction (AC) processors. MSI Level-1 images were processed with ACOLITE [72] (**I**), C2RCC (**I**, **II**, **IV**), C2X [70] (**IV**), POLYMER (**I**), and Sen2Cor [73] (**I**) AC processors. Detailed information on image downloading, processing steps, pixel quality control, and requirements for match-ups (**I**, **IV**, **V**) were described separately in each publication (**I**, **II**, **III**, **IV**, **V**).

### 3.4. OWT Classification

The aim of the classification was to ensure that every OWT was linked to specific bio-optical conditions in order to reflect on the dominance of individual or group OSC concentrations. Based on our experience, the blind clustering of the *in situ* measurement data was not giving desirable results as it was not linked to the physical properties of water. A previous study [41] presented the

OWT classification for boreal region lakes and linked the OWTs to the OSC concentrations, and the corresponding reflectance spectra were derived only for reference. The OWT classification (**I**) introduced in this thesis completes reflectance spectra from that study [41] with an understanding of how the OSC concentrations influence the shape of $R(\lambda)$ spectra. The developed OWT classification divides inland and coastal waters in the boreal region into five OWTs: Clear, Moderate, Turbid, Very Turbid, and Brown. The wavelength of the maximum, the slopes, and the amplitude of $R(\lambda)$ were chosen as key features, and the key aspects to distinguish between the OWTs were as follows:

- Spectra of the Clear and Moderate OWTs both had global maximum reflectance at wavelengths between 540 and 580 nm.
- For the Clear OWT, the reflectance at 500 nm was higher than at 650 nm, and it was higher than the reflectance at 500 nm for the Moderate OWT.
- The spectra of the Turbid OWT had a reflectance maximum between 580 and 605 nm, while the spectra of the Very Turbid OWT had a reflectance maximum at wavelengths between 685 and 715 nm.
- The spectra of the Brown OWT were characterized by a maximum in the red part of the spectrum and reflectance values below 0.006.

The OWT for each $R(\lambda)$ spectrum was determined by the maximum likelihood of individual spectra to OWT reference reflectance spectra, using spectral correlation similarity (SCS) and modified spectral angle similarity (MSAS), and was calculated as

$$\delta_j = 10(SCS + \frac{1-MSAS}{2}),$$

(3)

where SCS and MSAS are calculated as described by Homayouni and Roux [74] and $j$ denotes the OWT. The measured $R(\lambda)$ were classified into the OWT which has the highest $\delta$ value (**I, II, III, IV**).

Local sensitivity analysis was used to investigate the robustness of the OWT classification (**I**). Local sensitivity analysis shows how a small perturbation of input value influences the output value. The one-factor-at-a-time (OAT) method [75] was used in this study. The $R(\lambda)$ values in wavelength ranges of 400–500 nm, 500–700 nm, and 700–900 nm were considered as factors, and the perturbation range was set from –90% to +100%. Furthermore, additional sensitivity analyses were performed by using the OLCI and MSI bands as factors.

# 3.5. Retrieving Optical Water Quality Parameters

An OWT guided approach was used for finding models to estimate the optical water quality parameters, such as the concentration of Chl-a and TSM, $a_{CDOM}(442)$, and ZSD from $R(\lambda)$ spectra (**III**, **IV**). Since AC over inland and coastal waters is difficult and can contain large errors, in Paper **III**, the *in situ* measured $R(\lambda)$ spectra with 1 nm step resolution (Ramses) and for OLCI and MSI *in situ* measured $R(\lambda)$ convolved into OLCI and MSI bands using SRFs were used. 132 previously published algorithms, including 60 for Chl-a, 39 for TSM, 21 for CDOM, and 12 for ZSD, were tested to find the best model for each OWT. Details of the algorithms used are shown in Table A1 in Paper **III**. Repeated K-fold Cross-validation [76] was the statistical method used to build and select the model using published algorithms for the optical water quality parameter, and the R package caret [77] by Max Kuhn was used for imple-mentation. The ranking system used a combination of scaled and threshold-based statistical metrics to select the model for retrieving the optical water quality parameter from $R(\lambda)$ per OWTs. To also find the best solutions for the OLCI and MSI sensors' $R(\lambda)$ spectral scale, all calculations were made separately on the $R(\lambda)$ spectral scale with a 1 nm step, $R(\lambda)$ spectra convolved into OLCI sensor bands, and $R(\lambda)$ spectra convolved into MSI sensor bands.
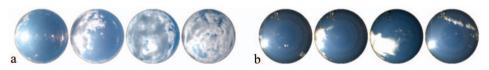
To look for the best solution to estimate optical water quality parameters in Baltic lakes using actual OLCI and MSI data (**IV**), either readymade products from different AC processors or band ratio algorithms using C2RCC, C2X, or top-of-atmosphere (TOA) reflectances were used to find the best method for each OWT. Thus, 42 different methods, including 16 for Chl-a, 9 for TSM, 5 for CDOM, and 12 for ZSD, were tested for OLCI and 66 different methods, including 21 for Chl-a, 14 for TSM, 10 for CDOM, and 21 for ZSD, were tested for MSI. Details of the methods used are shown in Table 1 in Paper **IV**.

# 4. RESULTS AND DISCUSSION

## 4.1. Impact of the Measurement Environment on the Variability of $R(\lambda)$

Uncertainties of *in situ* measured $R(\lambda)$ were lower between the 500–700 nm spectral ranges and lowest around 560 nm (Figure 1 in **V**). As $R(\lambda)$ depends on OSC concentrations, light conditions above the water surface, and water surface roughness [2], the impact of the measurement environment was studied with a logistic regression model (**I**) and PCA (**V**). According to the logistic regression model results, the wave height (p-value=0.007), wind speed (p-value=0.03), cloudiness (p-value=0.0005) and partial covering of the sun (p-value=0.02) were important parameters affecting the probability of a rise in the measurement uncertainty of $R(\lambda)$. Also, PCA results agreed that measurements with lower uncertainty were associated with lower wave height, lower wind speed, and good illumination conditions. In the measurement stations with high wind speed or waves, the shape of the $R(\lambda)$ spectrum remained the same; however, the values of $R(\lambda)$ varied strongly in all spectral areas (Table 1 in **I**). Whenever whitecaps started to appear on the water surface, the values of $R(\lambda)$ at shorter wavelengths increased and the shape of the $R(\lambda)$ spectrum changed.

In the measurement stations under changing cloud conditions, the $R(\lambda)$ usually started to vary, and data analysis was often difficult. For example, in the case shown in Figure 2(a), measurements started with an almost clear sky, although for 19 minutes, the whole sky contained clouds while the sun remained visible. The measured $R(\lambda)$ varied by 84% between 500–700 nm and by over 100% at shorter and longer wavelengths. However, the all sky camera images revealed that the presence of clouds did not always ruin the measurements. For example, in the case shown in Figure 2(b), clouds passed in front of the sun during the measurement, but they did not pass through the instrument's field of view (which is located at the top of the pictures). The variability of the radiance and irradiance measurements around 500 nm were 15% and 17.7%, respectively, while the deviation of $R(\lambda)$ stayed within 4.6%.
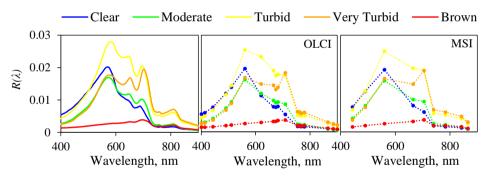


**Figure 2.** Changing cloud conditions during the $R(\lambda)$ measurements captured by all sky cameras in stations with (a) big and (b) small variability of $R(\lambda)$. Four images cover a time span of approximately 20 minutes (**I**).

## 4.2. Developed OWT Classification

The developed OWT classification (**I**) based on reflectance spectrum features divided inland and coastal waters into five classes: Clear, Moderate, Turbid, Very Turbid, and Brown. As shown in Figure 3, each OWT had a different $R(\lambda)$ spectra and was associated with a specific bio-optical condition.

The maximum $R(\lambda)$ of the Clear OWT occurred at wavelengths between 540 and 580 nm, and the absorption influence from OSC was lowest in the blue part of the spectrum compared to other OWTs. This OWT corresponds to water with low OSC concentrations and the highest water transparency. As for the Clear OWT, the maximum $R(\lambda)$ of the Moderate OWT occurred at wavelengths between 540 and 580 nm; however, the slope of $R(\lambda)$ was sharper in the Moderate OWT due to the larger influence of OSC absorption. The OSC concentrations increased, but none of them dominated.

In the Turbid OWT, the maximum $R(\lambda)$ was in the green part of the spectrum, and the values of $R(\lambda)$, between approximately 500 and 700 nm, were the highest of all OWTs. TSM was the dominant OSC in Turbid waters. In the Very Turbid OWT, the maximum $R(\lambda)$ occurred between 685 and 715 nm; this is due to the strong Chl-a peak which was associated with phytoplankton blooms. Chl-a was the dominant OSC in Very Turbid waters. The $R(\lambda)$ of the Brown OWT had very low values and reached the maximum in the red part of spectrum. Waters appeared dark or reddish and were dominated by CDOM.



**Figure 3.** $R(\lambda)$ for each OWT (left) and $R(\lambda)$ by OLCI, and MSI bands calculated with sensor-specific SRFs.

The spectral scales of both OLCI and MSI preserved key features of the OWT classification. For OLCI and MSI bands, the $R(\lambda)$ values of the OWTs were calculated using sensor-specific SRFs. OLCI has 21 bands, including four bands in the red part of the spectrum, where the Chl-a absorption peak is located. MSI was designed for the remote sensing of terrain and has a better spatial resolution; although it has fewer bands, it nevertheless captures differences in reflectance between the OWTs to a high degree. The well-placed spectral bands allow MSI to be successfully implemented in water monitoring. Although the
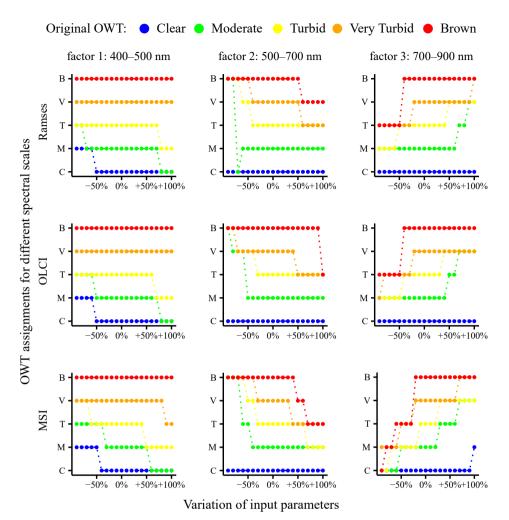
Moderate Resolution Imaging Spectroradiometer (MODIS) has a similar number of bands to MSI, the MODIS band central wavelengths are different; therefore, a strong maximum $R(\lambda)$ in the red part of the spectrum was no longer observed, and the reflectance spectra of the Turbid and Very Turbid OWTs were similar (Figure 2 in **I**).

### 4.2.1. Classification sensitivity

Sensitivity analyses (**I**) showed, as expected, that the OWT classification was sensitive to changes in the input $R(\lambda)$. The sensitivity of the determination of OWTs was influenced differently by the OWT, sensor type, and spectral range. Figure 4 shows a detailed local sensitivity analysis of the OWT results.

The Clear OWT was the most sensitive to a decrease of $R(\lambda)$ values in the wavelength range of 400–500 nm (local sensitivity factor 1). Changing the $R(\lambda)$ values in the wavelength range of 400–500 nm more than 40% caused the OWT to change to Moderate OWT. The Moderate OWT was sensitive to sensor type and spectral range. A decrease of $R(\lambda)$ values in the wavelength range of 400–500 nm or 500–700 nm (factor 2) could cause the spectra to be classified as Turbid, Very Turbid, or Brown. Regarding sensor type, for Ramses, a change of input parameter values of more than 60% was required to output a different OWT, while a change of just 20% was required for MSI.

The Turbid OWT was the most sensitive to changes in $R(\lambda)$ values in the wavelength range of 700–900 nm (factor 3). A decrease of factor 3 (e.g., 10% for MSI) changes the OWT to Moderate, while an increase of factor 3 changes the OWT into Very Turbid. The Very Turbid OWT was less sensitive to changes in the blue part of the spectrum and most sensitive to changes in the red part of the spectrum. The Brown OWT was sensitive to increases of factor 2 and decreases of factor 3. Changes of factor 1 had a minimal impact on the classification of the Brown OWT.
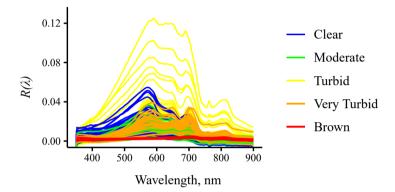
**Figure 4.** Local sensitivity analysis for OWT classification for sensors with different spectral scales. First row: Ramses; second row: OLCI; third row: MSI. Column 1: local sensitivity factor 1 (400–500 nm); column 2: factor 2 (500–700 nm); column 3: factor 3 (700–900 nm). The original OWTs are indicated by different colours (determined at parameter deviation of 0%), and the sensitivity analysis of OWT output is denoted as transitions between the OWTs. Input parameters vary from –90% to +100% on the x-axes (**I**).

Analysis treating satellite sensor bands as factors revealed that OLCI spectra were less sensitive to changes in input than MSI spectra. For OLCI spectra, the most sensitive OWT was Turbid when observed with bands 6 and 7, when a 30% change of input value would make an output OWT different. Usually, a change of input value of less than 70% does not change the classification assessment. MSI spectra were more sensitive to any input variation. This is especially true for MSI bands 3 and 5, where an input variation of more than

30% changes the designated OWT, except for the Clear and Moderate OWTs, where a variation of 70% and 20% is required to affect the classification result. However, Papers **I**, **IV**, and **V** showed that the variability in the *in situ* measured or satellite-derived $R(\lambda)$ can be more than 40% for certain spectral ranges.

## 4.3. OWT Classification Applied to *In Situ* Measured $R(\lambda)$

The classification of OWT applied on *in situ* measurements of $R(\lambda)$ at 180 stations (**I**) are shown in Figure 5, and the range of the variation of the OSC concentrations and ZSD for OWTs are shown in Table 2 in **I**. The OWT for each measurement station was determined by the maximum likelihood of an individual spectrum to type averages.
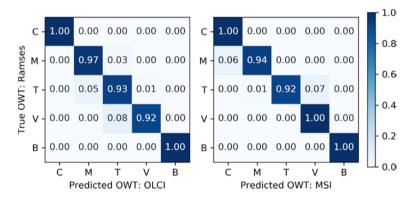


**Figure 5.** *In situ* measured $R(\lambda)$ classified into various OWTs by maximum likelihood calculated as (3) (**I**).

The Clear OWT was assigned to the $R(\lambda)$ of 39 measurement stations. The maximum of $R(\lambda)$ spectra was between 540 and 580 nm. These waters were the most transparent (maximum ZSD of 6.5 m) and with the lowest OSC concentrations. The Moderate OWT was assigned to the $R(\lambda)$ of 34 stations, with maximum similarly to the Clear OWT between 540 and 580 nm, with a slightly steeper slope in the blue part of the spectrum. OSC concentrations were slightly higher than for the Clear OWT; however, no particular OSC dominated over the others. The Turbid OWT was assigned to the $R(\lambda)$ of 76 stations. This OWT was dominated by TSM (maximum TSM of 62.4 mg·l$^{-1}$) and had the highest absolute values of the $R(\lambda)$ of all the OWTs; however, the maximum value of $R(\lambda)$ varied greatly within this OWT.

The Very Turbid OWT was assigned to the $R(\lambda)$ of 24 stations. These spectra had a maximum in the red part of the spectrum and showed a clear Chl-a peak. These stations were dominated by Chl-a (maximum value of 71.8 mg·m$^{-3}$). The Brown OWT was the least frequent of all OWTs, being assigned to the $R(\lambda)$ of seven stations. These stations had very low $R(\lambda)$ values (under 0.005), having a

maximum in the red part of the spectrum, and were dominated by CDOM (CDOM values at 380 nm of between 4.3 and 14.7 $m^{-1}$).

The accuracies of OWT estimations, based on *in situ* measurements of $R(\lambda)$ convolved into OLCI and MSI sensor bands using sensor-specific SRFs, were 95% for both. As the goal was to develop an OWT classification that could be used in an OWT guided approach to retrieve optical water quality parameters from OLCI and MSI data, it was important to understand the capability to assign the same OWT based on *in situ* measurements of $R(\lambda)$ regardless of spectral scale (Ramses, and OLCI and MSI bands). Confusion matrices were constructed between the OWTs assigned based on *in situ* measurements of $R(\lambda)$ (set as the true OWT value) and those which were assigned based on *in situ* measurements of $R(\lambda)$ convolved into OLCI and MSI sensor bands (set as the predicted OWT value). As shown in Figure 6, the OLCI confusion matrix illustrates that a strong distinction was made between the Clear and Brown OWTs (100% correct assignment), while the lowest assignment accuracy (92%) was observed for the Very Turbid OWT, with 8% of spectra being misclassified as Turbid. The MSI confusion matrix demonstrates a strong distinction for the Clear, Very Turbid, and Brown OWTs (100% correct assignment); however, some Turbid spectra were misclassified as Very Turbid (7%) and Moderate (1%).



**Figure 6.** Normalized confusion matrices showing the accuracy of OWT assignment using *in situ* measurements of $R(\lambda)$ convolved into OLCI, and MSI bands. Rows show the true OWTs determined from *in situ* measurements of $R(\lambda)$ using Ramses, and columns show the predicted OWTs determined from the convolved $R(\lambda)$. The diagonal elements represent situations in which the predicted OWT is the same as the true OWT (i.e., correct classification).

## 4.4. OWT Guided Approach

In Paper **III,** the OWT guided approach for boreal region inland and coastal waters was introduced to estimate optical water quality parameters, such as the concentration of Chl-a and TSM, $a_{CDOM}(442)$, and ZSD, from hyperspectral,

OLCI, and MSI reflectance data. 132 various published empirical algorithms (Tabel A1 in **III**) were tested to find the best algorithm for every OWT for different spectral scales for different optical water quality parameters. As the *R(λ)* spectra are the basis for all future calculations and developments, the error in *R(λ)* may multiply in the final product or lead to incorrect conclusions [78]. Moreover, it is known that AC over inland and coastal areas is difficult [79–81], and the result still can contain large errors (**I**, **IV**) [31,82,83]. Therefore, we used *in situ* measured reflectance spectra and *in situ* measured reflectance spectra convolved into OLCI and MSI bands using sensor SRFs. However, it is still important to remember that *in situ* measured *R(λ)* is not the absolute truth and can contain large errors (**I**, **IV**, **V**) [84]. Development was based on data from 51 Estonian and Finnish lakes and from the Baltic Sea coastal area, altogether 415 *in situ* measurement stations, which covered a wide range of variation of optical water quality parameters (Chl-a: 0.5–215.2 mg·m$^{-3}$; TSM: 0.6–46.0 mg·L$^{-1}$; $a_{CDOM}$(442): 0.4–43.7 m$^{-1}$; and ZSD: 0.2–12.2 m).
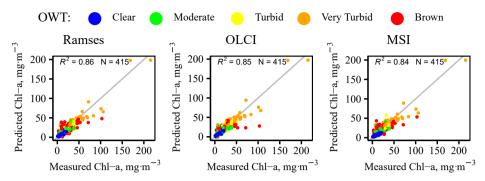
### 4.4.1. Predictive Models for Concentration of Chl-a

For Chl-a, 60 published empirical algorithms were tested to retrieve the concentration of Chl-a from the *R(λ)* spectra, and the best models for each OWT and each spectral scale, such as Ramses, and OLCI and MSI bands, were defined in Table 1. The linear regression models showed better performance in all cases. Compared to other optical water quality parameter model selections, Chl-a models varied the most between OWTs and the spectral scales. The widely used [10,85–92] ratio 700/670 nm, with a high correlation for high-biomass waters, was the best model only for Turbid OWT with a Ramses spectral scale. However, the two-variable ratio models were the best for all the spectral scales in Brown OWT, for OLCI and MSI in Moderate OWT, for Ramses in Turbid OWT, and for MSI in Very Turbid OWT. In our best-performing models, all variables were selected from the red and NIR spectral range, with different combinations. Moreover, broadly used [10,31,86,93–95] algorithms that include chlorophyll fluorescence information using values of reflectance spectra around 681 nm were not the best in any cases. For Brown OWT, retrieving the concentration of Chl-a from *R(λ)* was the most difficult, and the coefficient of determination suggested that the regression model explained about 40% of the variance observed in the *in situ* measured data; this needs future investigation and improvement. The correlations shown in Figure 7 between the concentration of Chl-a predicted using OWT based models and the *in situ* measured concentration of Chl-a were strong, such as 0.93 for Ramses and OLCI and 0.92 for MSI.

**Table 1.** The best published Chl-a predictive models tested in this thesis for each OWT and for sensors with different spectral scales. Descriptions of the algorithms used for these models are found in Table A1 in Paper **III**. The band central wavelength is used to mark the OLCI and MSI models' bands.

| OWT | Model Formula | $R^2$ | AR[1] |
|---|---|---|---|
| **Ramses** | | | |
| Clear | $Chla = 5956.0 \cdot \left(R709 - \dfrac{R665 + R754}{2}\right) + 3.84$ | 0.79 | [96] |
| Moderate | $Chla = -84.42 \cdot \left(\left(\dfrac{1}{R705} - \dfrac{1}{R665}\right) \middle/ \left(\dfrac{1}{R705} + \dfrac{1}{R665}\right)\right) + 18.69$ | 0.62 | [97] |
| Turbid | $Chla = 55.85 \cdot \left(\dfrac{R702}{R674}\right) - 43.08$ | 0.79 | [92] |
| Very Turbid | $Chla = -180.6 \cdot \left(\left(\dfrac{1}{R705} - \dfrac{1}{R665}\right) \middle/ \left(\dfrac{1}{R705} + \dfrac{1}{R665}\right)\right) + 19.89$ | 0.88 | [97] |
| Brown | $Chla = 46.56 \cdot \left(\dfrac{R748}{R667}\right) - 8.310$ | 0.41 | [91] |
| **OLCI** | | | |
| Clear | $Chla = 6097.2 \cdot \left(R708.75 - \dfrac{R665 + R753.75}{2}\right) + 3.998$ | 0.78 | [96] |
| Moderate | $Chla = -33.91 \cdot \left(\dfrac{R673.75}{R708.75}\right) + 54.07$ | 0.67 | [31] |
| Turbid | $Chla = 177.4 \cdot \left(\dfrac{1}{R673.75} - \dfrac{1}{R708.75}\right) \cdot R753.75 + 20.68$ | 0.79 | [98] |
| Very Turbid | $Chla = -173.6 \cdot \left(\left(\dfrac{1}{R708.75} - \dfrac{1}{R665}\right) \middle/ \left(\dfrac{1}{R708.75} + \dfrac{1}{R665}\right)\right) + 25.6$ | 0.89 | [97] |
| Brown | $Chla = 42.96 \cdot \left(\dfrac{R753.75}{R665}\right) - 5.470$ | 0.38 | [91] |
| **MSI** | | | |
| Clear | $Chla = 4367.1 \cdot \left(R705 - R665 - \dfrac{705 - 665}{740 - 665} \cdot (R740 - R665)\right) + 2.658$ | 0.61 | [95] |
| Moderate | $Chla = -40.83 \cdot \left(\dfrac{R665}{R705}\right) + 61.71$ | 0.60 | [31] |
| Turbid | $Chla = -184.1 \cdot \left(\dfrac{R740}{R705} - \dfrac{R740}{R665}\right) + 21.20$ | 0.63 | [11] |
| Very Turbid | $Chla = -171.4 \cdot \left(\dfrac{R665}{R705}\right) + 183.6$ | 0.89 | [31] |
| Brown | $Chla = 46.98 \cdot \left(\dfrac{R740}{R665}\right) - 9.360$ | 0.40 | [91] |

[1] Algorithm reference.

**Figure 7.** Comparison of concentrations of Chl-a estimated from *in situ* measured *R(λ)* spectra using the OWT guided approach and *in situ* measured concentrations of Chl-a for different spectral scales: (left to right) Ramses, OLCI, and MSI. OWTs are indicated by colours, and the line shows a 1:1 relationship (**III**).
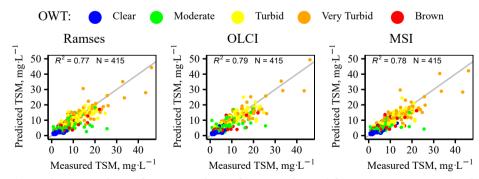
## 4.4.2. Predictive Models for Concentration of TSM

For TSM, 39 published  empirical algorithms were tested to retrieve the concentration of TSM from the *R(λ)* spectra, and the best models for each OWT and each spectral scale were defined in Table 2. The model using the Kutser *et al*. [99] algorithm, based on a reflectance peak at 810 nm, was the best for MSI for Turbid, Very Turbid, and Brown OWTs. It also suited the Ramses and OLCI Turbid, Very Turbid, and Brown OWTs. Similarly, previous studies [100–102] have pointed out the usefulness of the NIR spectral part for retrieving the TSM in turbid waters with high amounts of mineral particles. However, despite being developed in waters with high amounts of mineral particles, Kutser *et al*. [99] showed the usefulness of the NIR part of the spectra in waters where the majority of TSM was organic, as in our dataset. For the Clear OWT, the model using Zhang *et al*. [103], a developed log-transformed multiple linear regression algorithm based on a combination of 488, 555, and 645 nm information, was the best for all sensors. Zhang *et al*. [103] demonstrated that reflectance at 550 nm is sensitive to TSM changes in less turbid waters and reflectance at 645 nm is sensitive in turbid waters. The correlations between concentrations of TSM predicted using OWT based models and *in situ* measured concentrations of TSM values were strong: 0.87, 0.89, 0.88 for Ramses, OLCI, and MSI respectively. The Moderate OWT had the lowest coefficient of determination for all the spectral scales from all the OWTs, and as shown in Figure 8, that model for Moderate OWT tends to strongly underestimate points with high TSM values (from 15 to 25 mg·L$^{-1}$).

**Table 2.** The best published TSM predictive models tested in this thesis for each OWT and for sensors with different spectral scales. Descriptions of the algorithms used for these models are found in Table A1 in Paper **III**. The band central wavelength is used to mark the OLCI and MSI models' bands.

| OWT | Model Formula | $R^2$ | AR[1] |
|---|---|---|---|
| **Ramses** | | | |
| Clear | $\log TSM = -30.20 \cdot R555 + 74.14 \cdot R645 - 0.991 \cdot \frac{R488}{R555} + 0.784$ | 0.47 | [103] |
| Moderate | $\log TSM = 0.264 \cdot \log R555 + 14.71 \cdot R645 - 0.189 \cdot \log \frac{R488}{R555} + 0.941$ | 0.36 | [104] |
| Turbid | $\ln TSM = 0.685 \cdot \ln \frac{R620 \cdot R681}{R510} + 4.852$ | 0.69 | [105] |
| Very Turbid | $TSM = 3748.6 \cdot \left(R810 - \frac{R770 + R840}{2}\right) + 5.515$ | 0.68 | [99] |
| Brown | $TSM = 5673.9 \cdot \left(R810 - \frac{R770 + R840}{2}\right) + 2.178$ | 0.61 | [99] |
| **OLCI** | | | |
| Clear | $\log TSM = -24.36 \cdot R560 + 80.66 \cdot R665 - 1.096 \cdot \frac{R490}{R560} + 0.840$ | 0.47 | [103] |
| Moderate | $TSM = -8090.1 \cdot \left(R865 - \frac{R778.75 + R865}{2}\right) + 1.825$ | 0.45 | [99] |
| Turbid | $TSM = -7664.9 \cdot \left(R865 - \frac{R778.75 + R865}{2}\right) + 3.250$ | 0.69 | [99] |
| Very Turbid | $\log TSM = -0.249 \cdot \log R560 + 26.20 \cdot R665 - 0.483 \cdot \log \frac{R490}{R560} + 0.095$ | 0.60 | [104] |
| Brown | $\ln TSM = 311.8 \cdot \left(R708.75 - \frac{R753.75 + R665}{2}\right) + 1.165$ | 0.49 | [106] |
| **MSI** | | | |
| Clear | $\log TSM = -24.0 \cdot R560 + 79.02 \cdot R665 - 1.152 \cdot \frac{R490}{R560} + 0.892$ | 0.49 | [103] |
| Moderate | $\log TSM = 0.279 \cdot \log R560 + 16.24 \cdot R665 - 0.215 \cdot \log \frac{R490}{R560} + 0.958$ | 0.36 | [104] |
| Turbid | $TSM = 7037.6 \cdot \left(R783 - \frac{R783 + R865}{2}\right) + 3.464$ | 0.64 | [99] |
| Very Turbid | $TSM = 5416.1 \cdot \left(R783 - \frac{R783 + R865}{2}\right) + 6.259$ | 0.68 | [99] |
| Brown | $TSM = 7573.5 \cdot \left(R783 - \frac{R783 + R865}{2}\right) + 2.748$ | 0.54 | [99] |

[1] Algorithm reference.



**Figure 8.** Comparison of concentrations of TSM estimated from *in situ* measured $R(\lambda)$ spectra using the OWT guided approach and *in situ* measured concentrations of TSM for sensors with different spectral scales: (from left) Ramses, OLCI, and MSI. OWTs are indicated by colours, and the line shows a 1:1 relationship (**III**).
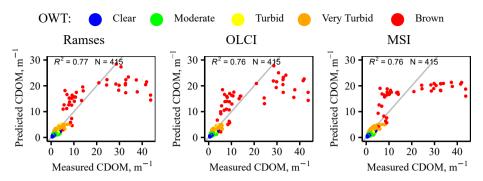
### 4.4.3. Predictive Models for Absorption Coefficient of CDOM

For $a_{CDOM}(442)$, 21 published empirical algorithms were tested to retrieve $a_{CDOM}(442)$ values from the $R(\lambda)$ spectra, and the best models for each OWT and for each spectral scale were defined in Table 3. The power regression models (referred also as a log–log regression model) of the reflectance ratio showed better performance for all the spectral scales in the Clear, Moderate, and Turbid OWTs. For instance, the reflectance ratio 665/560 nm was the best for OLCI and MSI; however, for Ramses, the model using the ratio 560/660 nm was preferred. These ratios are quite commonly used for predictions; however, they are used with different statistical techniques, such as linear regression [85,90,107–109] and power regression [107–110]. For the Brown OWT, the log-transformed multiple linear regression model using the Brezonik *et al.* [111] algorithm, using 488 nm and 830 nm, showed the highest results for all spectral scales. However, Figure 9 shows that the capability to estimate the Brown OWT high CDOM values over 20 m$^{-1}$ was non-existent. Therefore, future work is needed to find or develop algorithms that are suitable for this kind of humic water. Since uncertainties of $R(\lambda)$ in the Brown OWT were higher in the blue part of the spectrum, the longer wavelengths would be recommended as preferred for algorithms.

**Table 3.** The best published CDOM predictive models tested in this study for each OWT and for sensors with different spectral scales. Descriptions of the algorithms used for these models are found in Table A1 in Paper **III**. The band central wavelength is used to mark the OLCI and MSI models' bands.

| OWT | Model Formula | $R^2$ | AR [1] |
|---|---|---|---|
| **Ramses** | | | |
| Clear | $\ln CDOM = -1.4124 \cdot \ln\left(\frac{R560}{R660}\right) + 1.042$ | 0.74 | [109] |
| Moderate | $\ln CDOM = -1.470 \cdot \ln\left(\frac{R570}{R655}\right) + 1.111$ | 0.36 | [110] |
| Turbid | $\ln CDOM = -2.187 \cdot \ln\left(\frac{R570}{R655}\right) + 1.225$ | 0.45 | [110] |
| Very Turbid | $CDOM = 3.063 \cdot \frac{R664}{R550} + 1.096$ | 0.42 | [85] |
| Brown | $\ln CDOM = -107.8 \cdot R485 - 0.245 \cdot \frac{R485}{830} + 3.371$ | 0.38 | [112] |
| **OLCI** | | | |
| Clear | $\ln CDOM = 1.352 \cdot \ln\left(\frac{R665}{R560}\right) + 1.070$ | 0.74 | [108] |
| Moderate | $\ln CDOM = 1.108 \cdot \ln\left(\frac{R665}{R560}\right) + 1.070$ | 0.33 | [108] |
| Turbid | $\ln CDOM = 1.490 \cdot \ln\left(\frac{R665}{R560}\right) + 1.265$ | 0.32 | [108] |
| Very Turbid | $CDOM = 3.128 \cdot \frac{R665}{R560} + 1.266$ | 0.38 | [85] |
| Brown | $\ln CDOM = -127.6 \cdot R485 - 0.140 \cdot \frac{R485}{830} + 3.377$ | 0.41 | [112] |
| **MSI** | | | |
| Clear | $\ln CDOM = 1.429 \cdot \ln\frac{R665}{R560} + 1.059$ | 0.74 | [108] |
| Moderate | $\ln CDOM = 1.330 \cdot \ln\frac{R665}{R560} + 1.086$ | 0.42 | [108] |
| Turbid | $\ln CDOM = 1.338 \cdot \ln\frac{R665}{R560} + 1.151$ | 0.31 | [108] |
| Very Turbid | $CDOM = 3.292 \cdot \frac{R665}{R560} + 0.947$ | 0.39 | [85] |
| Brown | $\ln CDOM = -62.93 \cdot R665 - 0.020 \cdot \frac{R560}{R490} + 3.107$ | 0.41 | [113] |

[1] Algorithm reference.

**Figure 9.** Comparison of $a_{\text{CDOM}}(442)$ estimated from the *in situ* measured $R(\lambda)$ spectra using the OWT guided approach and *in situ* measured $a_{\text{CDOM}}(442)$ for sensors with different spectral scales: (from left) Ramses, OLCI, and MSI. OWTs are indicated by colours, and the line shows a 1:1 relationship (**III**).
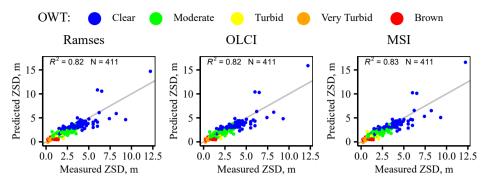
### 4.4.4. Predictive Models for ZSD

For ZSD, 12 published empirical algorithms were tested to retrieve ZSD from the $R(\lambda)$ spectra. The best models for each OWT and for each sensor with different spectral scales are defined in Table 4. The model using the Kloiber *et al*. [114] algorithm based on log-transformed multiple regression of form 485/660 nm ratio and the additional 485 nm, was the best model for all spectral scales in the Clear, Moderate, and Turbid OWTs. The algorithm was developed for values up to 5 m, and 96% of the Clear, Moderate and Turbid OWT measurements fitted within the limits. However, the maximum measured ZSD in our dataset was 12.2 m and was measured during an upwelling event in the Gulf of Finland. Also, Figure 10 shows a lower accuracy predicting high ZSDs. However, studies [112,115] have demonstrated that this algorithm can be used up to 15 m. Therefore, the optically extreme and different conditions of the upwelling can be the reason for the lower prediction accuracy. For the Brown OWT, retrieving ZSD from $R(\lambda)$ was the most difficult, and the coefficient of determination was around 0.28 for the best model based on reflectance at 660 nm. Also, Matthews [102] suggested a single band algorithm for humic lakes. Overall, the Brown OWT models need future work.

**Table 4.** The best ZSD predictive models using published algorithms tested in this thesis for each OWT and for sensors with different spectral scales. Descriptions of the algorithms used for these models are found in Table A1 in Paper **III**. The band central wavelength is used to mark the OLCI and MSI models' bands.

| OWT | Model Formula | $R^2$ | AR[1] |
|---|---|---|---|
| **Ramses** | | | |
| Clear | $\ln ZSD = 0.617 \cdot \dfrac{R485}{R660} - 43.58 \cdot R485 + 0.759$ | 0.60 | [114] |
| Moderate | $\ln ZSD = 1.685 \cdot \dfrac{R485}{R660} - 63.01 \cdot R485 - 0.265$ | 0.64 | [114] |
| Turbid | $\ln ZSD = 2.98 \cdot \dfrac{R485}{R660} - 41.32 \cdot R485 - 1.294$ | 0.74 | [114] |
| Very Turbid | $ZSD = -5.63e^{-07} \cdot \dfrac{\ln R555}{R488} - 0.018 \cdot \dfrac{R645 + R858}{R469} - 15.57 \cdot R555 + 1.07$ | 0.48 | [116] |
| Brown | $\ln ZSD = 0.268 \cdot \ln R660 + 1.024$ | 0.27 | [117] |
| **OLCI** | | | |
| Clear | $\ln ZSD = 0.573 \cdot \dfrac{R490}{R665} - 42.89 \cdot R490 + 0.742$ | 0.62 | [114] |
| Moderate | $\ln ZSD = 1.801 \cdot \dfrac{R490}{R665} - 60.42 \cdot R490 - 0.510$ | 0.65 | [114] |
| Turbid | $\ln ZSD = 2.960 \cdot \dfrac{R490}{R665} - 39.95 \cdot R490 - 1.451$ | 0.69 | [114] |
| Very Turbid | $ZSD = -7.03e^{-06} \cdot \dfrac{\ln R560}{R490} - 0.027 \cdot \dfrac{R645 + R858}{R469} - 14.63 \cdot R555 + 1.08$ | 0.48 | [116] |
| Brown | $\ln ZSD = 0.269 \cdot \ln R665 + 1.037$ | 0.28 | [117] |
| **MSI** | | | |
| Clear | $\ln ZSD = 0.602 \cdot \dfrac{R490}{R665} - 45.09 \cdot R490 + 0.728$ | 0.64 | [114] |
| Moderate | $\ln ZSD = 1.821 \cdot \dfrac{R490}{R665} - 63.25 \cdot R490 - 0.478$ | 0.68 | [114] |
| Turbid | $\ln ZSD = 2.784 \cdot \dfrac{R490}{R665} - 38.22 \cdot R490 - 1.367$ | 0.63 | [114] |
| Very Turbid | $ZSD = -6.81e^{-06} \cdot \dfrac{\ln R560}{R490} - 0.030 \cdot \dfrac{R645 + R858}{R469} - 17.11 \cdot R555 + 1.14$ | 0.51 | [116] |
| Brown | $\ln ZSD = 0.271 \cdot \ln R665 + 1.033$ | 0.29 | [117] |

[1] Algorithm reference.

**Figure 10.** Comparison of ZSD estimated from *in situ* measured *R(λ)* spectra using the OWT guided approach and *in situ* measured ZSD for sensors with different spectral scales: (from left) Ramses, OLCI, and MSI. OWTs are indicated by colours, and the line shows a 1:1 relationship (**III**).

## 4.5. OWT Guided Approach Implementation with Satellite Data

### 4.5.1. Selection of AC Processor

Accurate AC over inland and coastal areas is difficult [79–81], and at the moment, there is no one universally correct choice. Therefore, it is necessary to select the best available AC processor for the region of interest and for the sensor of interest. However, it is important to keep in mind that AC processors are constantly developed and improved; therefore, aspects of the suitable AC processor for the region of interest can change quickly. Generally, the green bands were estimated most accurately, and the blue bands had the highest deviations (**I**, **IV**, **V**). In Paper **I**, the C2RCC AC processor was suggested for both MSI and OLCI based on available *R(λ)* match-ups.

For OLCI image match-ups, the values of *R(λ)* derived from images processed with ALTNN and C2RCC AC processors were more accurate than those derived from images processed with the standard L2 AC processor. L2 strongly underestimated *R(λ)* at short wavelengths, sometimes even giving negative values; however, the L2 AC processor was the best to capture the maximum in the red part of spectrum in the Very Turbid OWT (Figure 8 in **I**).

Comparison of OWTs determined based on *in situ* measured *R(λ)* and OWTs determined using *R(λ)* derived from OLCI images processed with different ACs showed that the C2RCC had the highest classification accuracy. L2 had the lowest classification accuracy for OWTs; the Very Turbid or Brown OWT was assigned mainly because the first maximum of *R(λ)* at 550–580 nm was strongly underestimated, and therefore the resulting spectral shape of *R(λ)* was distorted. Moreover, sensitivity analyses confirmed that a decrease of the *R(λ)* values at 500–700 nm caused Moderate and Turbid OWTs to be assigned as Very Turbid or Brown.

For MSI match-up points away from the shore, the C2RCC, POLYMER, and Sen2Cor AC processors gave quite similar values of $R(\lambda)$, while the ACOLITE AC processor commonly overestimated $R(\lambda)$. However, C2RCC was not able to capture the maximum $R(\lambda)$ in the red part of the spectrum. For small lakes, AC processors' values of $R(\lambda)$ differed more (Table A1 in **I**), and in some cases, AC processors did not provide any results. For example, only the C2RCC AC processor was able to derive data for small humic lakes.

Comparison between OWTs obtained from *in situ* measured $R(\lambda)$ and OWTs obtained from MSI images processed with different ACs (Table A1 and Figure 7 in **I**) showed that POLYMER had the highest number of correct classifications; however, the C2RCC AC processor was suggested for MSI since POLYMER was not able to retrieve $R(\lambda)$ for 43% of match-ups.

In Paper **IV**, for MSI, the C2X AC processor was suggested for Baltic lakes based on available $R(\lambda)$ match-ups. Comparison of the spectral bands, the visual inspection of the general shape of spectra (Figures A2-A4 in **IV**), and accuracy of derived OWTs (72%) were the basis for the decision. For OLCI, the C2RCC AC processor was used similarly, as suggested in Paper **I**. In Paper **V**, the newly tested POLYMER AC processor was suggested for Estonian inland and coastal waters for OLCI images based on available $R(\lambda)$ match-ups (Table 3 in **V**). Similarly, in Paper **I**, it was noted that the agreement between the AC processors increased further away from the shore.

## 4.5.2. Comparability of OWTs

The two satellite sensors, OLCI and MSI, generally agreed on the dominant OWT (**II**) in the studied Latvian and Estonian lakes based on all the valid pixels of the cloud-free scenes of the lakes during 2017 (152 OLCI and 45 MSI images) (Figure 2 and Table 2 in **II**). The Latvian shallow, brown-water Lake Burtnieks [118] was dominated by the Brown OWT. The Turbid OWT was dominant in Lake Lubans and Lake Võrtsjärv and the Clear OWT in Lake Razna. However, the distributions of non-dominant OWTs differ on sensors. For example, in Lake Võrtsjärv, 91% of the pixels in OLCI images were determined as the Turbid OWT, but in MSI images, 50% of the pixels were determined as the Turbid OWT. Overall, MSI data showed more variability in different OWTs, while OLCI tended to be homogenous in the OWTs.
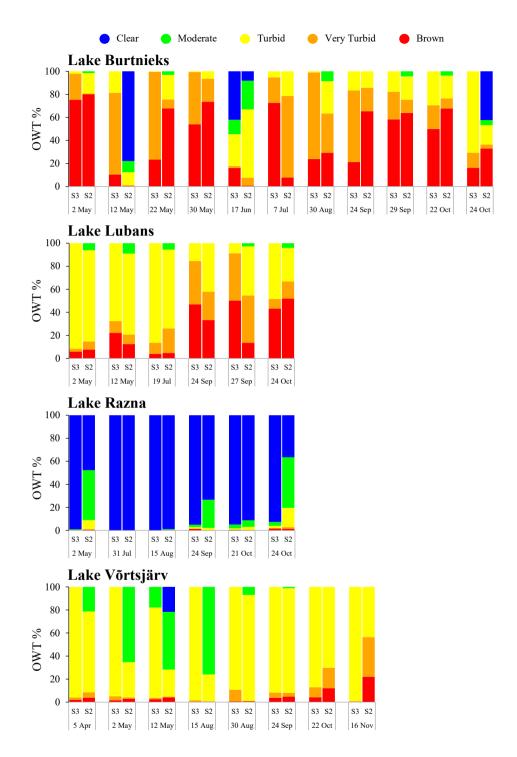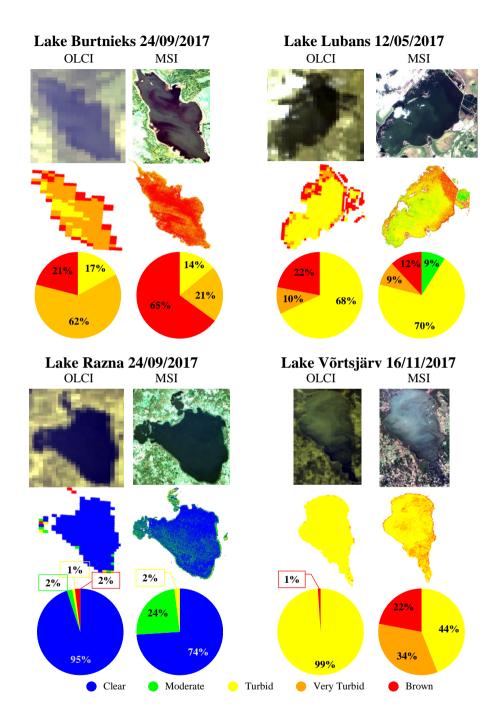
**Figure 11.** The distribution of OWTs for all OLCI (S3) and MSI (S2) matching cases (**II**).

31 cases with both OLCI and MSI cloud-free images from the same day were analyzed to compare lakes' OWTs derived from OLCI and MSI images (**II**). As shown in Figure 11, the best agreement between the two sensors' distribution of the OWTs were in Lake Razna and Lake Lubans. The most disagreements in determining the OWT were in Lake Võrtsjärv, where in half of the matching days, there were the differences between OWTs determined from OLCI and MSI images. Since the determination of OWTs depended on $R(\lambda)$ derived from satellite sensor images, AC can impact the result of retrieval of the OWTs. AC over inland and coastal waters is challenging because about 90% of the signal received by the sensor is not affected by the water itself [119]. Even though the same C2RCC AC processor was used for both sensors, the sensors have different spectral scales, and sensitivity analysis of OWT classification (**I**) showed that MSI was more sensitive to changes in input reflectance. The correlation between prevalent OWT derived from OLCI and MSI images was 0.74 (without outlier: 0.87) (Figure 4 in **II**).

### 4.5.3. Spatial and Temporal Variability of OWTs

OLCI and MSI spatial and temporal resolution are some of the advantages that remote sensing capabilities have over traditional *in situ* monitoring to monitor water quality in inland and coastal waters. As shown in Figure 12, the MSI with higher spatial resolution was able to monitor finer patterns and also smaller lakes. Generally, for Lake Burtnieks, both sensors agreed on the spatial variability of the OWTs but quite often disagreed on the OWT itself. Lake Burtnieks is a brown-water lake with frequent heavy blooms [120], which can lead to quickly changing spatial variability of the OWT. In the case of Lake Võrtsjärv, the water was homogeneous according to the OLCI data. Additionally, the literature describes the lake as having homogenous waters, meaning that a single measurement point describes 90% of the lake [121]. However, the OWT determined from MSI images demonstrated fine patterns of different OWTs. Typically, the narrow southern part had a Very Turbid and Brown OWTs, and the northern part was classified into Moderate, Turbid, and some Very Turbid OWTs. The pattern of spatial variation of OWTs from the MSI images agrees with the characteristics of the lake bottom [122]. The most agreement between both satellites was found in Lake Razna.

**Figure 12.** Comparison of the spatial variability of OWTs between OLCI and MSI in four different lakes on selected dates. The upper row for each lake shows the enhanced true colour images, the second shows the spatial variability of the OWTs, and the third row shows the percentages of each OWT of the given scene (**II**).
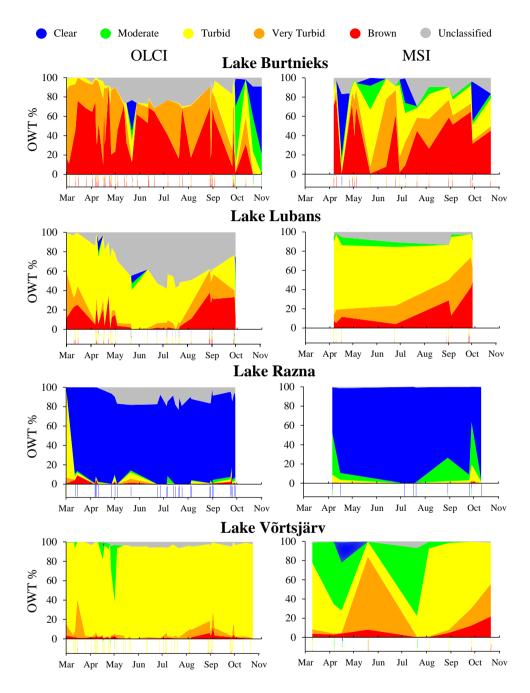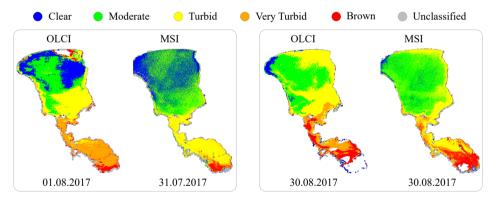
**Figure 13.** Temporal variability and the distribution of OWTs derived from OLCI and MSI in different lakes during 2017. The lower panel of each sub-figure shows the frequency of the acquired data (**II**).

The temporal variability of the OWT distributions in Figure 13 illustrates a change in the lake optical properties during one ice-free period (**II**). In Lake Burtnieks, the OWTs changed quite rapidly from the Brown to Very Turbid OWT or *vice versa*. That was most likely due to fluctuations in concentrations of Chl-a or the combination of water level fluxes and intensive agriculture [120]. Additionally, for the CDOM-rich water, the AC was difficult to perform well, and over- or underestimation of deriving $R(\lambda)$ from satellite images can exceed classification sensitivity and can lead to misclassification of OWTs.

Lake Lubans and Lake Razna showed more stability of the OWTs and a similar pattern. The influence of infrequent data was shown most clearly on Lake Võrtsjärv, where the overall temporal variability was affected by one June MSI image (Figure 13). Since there were 47 OLCI images and only 9 MSI images from Lake Võrtsjärv over 2017, the MSI one-day image had more proportional weight in the result. As shown in Figure 13, using fewer than 10 images per year made the temporal variability analysis of OWTs in dynamic water bodies quite unreliable. However, in monitoring programs, conclusions are often made about water conditions with even lower temporal resolution. From over 2000 Latvian lakes, only a small part of them are monitored monthly, and nearly 300 lakes have just one sampling during a 3-year period [123]. In Estonia, from over 2300 lakes, only Lake Võrtsjärv is monitored monthly. Twelve other lakes are monitored up to five times per year. There are 90 other lakes that are monitored up to twice over a five-year period [124].
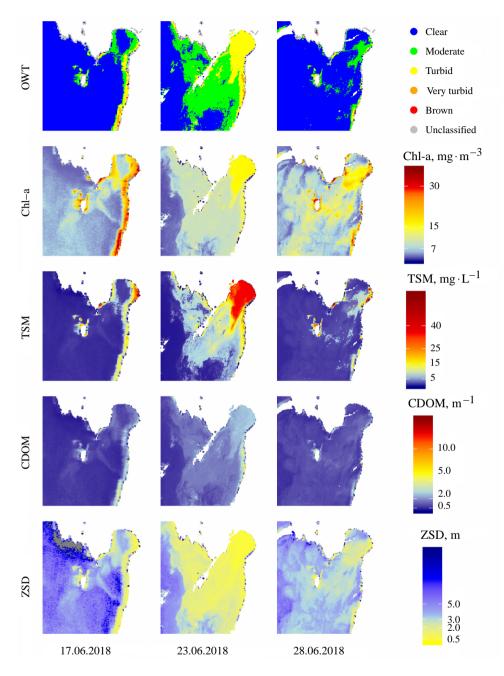


**Figure 14.** Examples of temporal variability and the distribution of OWTs derived from OLCI and MSI in Lake Peipus during 2017.

In Lake Peipus, all OWTs were present throughout the season, but the distribution of OWTs changed. The lake is a large, shallow, optically complex, and very dynamic water body, and it has a strong north–south OSC concentration gradient. In mid-summer, the OSC concentrations in the northern part of Lake Peipus were lower, and its waters were mainly classified as the Clear or Moderate OWTs. At the same time, water in the narrower southern part of Lake

Peipus was classified as the Turbid OWT on MSI and Very Turbid OWT on OLCI images. At the end of August when OSC concentrations increase, the waters were more widely classified as Turbid OWT in the northern part of Lake Peipus and as Brown OWT in the southern part. As shown on Figure 14, the variation in OWTs obtained with MSI and OLCI images (**I**) was similar to that obtained in Paper **VI**, in which OWT classification [41] was performed based on OSC concentrations. Overall, the dynamics of OWTs obtained from MSI and OLCI images are comparable.

## 4.5.4. Detecting Ecosystem Changes by Using the OWT Guided Approach (an example)

The OWT guided approach to estimate optical water quality parameters was applied to OLCI images acquired in the Pärnu Bay region to investigate ecosystem seasonal and spatial changes and responses to weather effects. As shown in Figure 15, the left column includes OWT estimations and optical water quality parameters derived images taken during the most common situations when higher values were present close to the coast; however, the bay was mainly classified into the Clear OWT. There was a storm event with a daily average wind speed of 11.2 m·s$^{-1}$ and gusts over 21 m·s$^{-1}$ on 22 June 2018. The image captured the day after the storm showed the changes in the bay. As the bay is shallow with a soft bottom, the wind caused resuspension of sediments into the water column, and as a result, the bay was then classified into the Turbid or Moderate OWTs. Derived images (Figure 15) showed an increase of TSM concentration (due to both inorganic and organic particulates) and a drastic decrease in ZSD. This indicates changes in the underwater light field. The Chl-a values rose, but we do not have a reason to believe that this was actually true in this case, and we assume the overprediction of the Chl-a due to a TSM side-effect. Firstly, finding empirical algorithms that effectively separate the signals from TSM and Chl-a can be challenging [102], and secondly, the datasets used to develop this approach mainly include TSM dominated by SPOM *in situ* measurements. In the future, it is necessary to add more SPIM-dominated *in situ* measurements to train our Turbid OWT models. Five days later (right column of Figure 15), conditions had returned to near those on the 17th, although with higher Chl-a values, possibly due to due to added nutrients from the sediments. These changes are quick in nature and often remain uncaptured by traditional monitoring programs, adding more value to remote sensing possibilities.

**Figure 15**. Changing OWTs and optical water quality parameters (such as the Chl-a, TSM, CDOM, and ZSD) before and after a strong wind (day average wind speed 11.2 m·s-1 and the gust over 21 m·s-1) event on 22 June 2018 in Pärnu Bay, captured by OLCI images processed with the C2RCC AC processor. Water quality parameters are estimated from $R(\lambda)$ using OWT based algorithms (**III**).

# 5. CONCLUSIONS

- The uncertainties of *in situ* measured $R(\lambda)$ were lower, between 500–700 nm. The wave height, wind speed, and changing illumination conditions were important parameters affecting the probability of a rise in the measurement uncertainty of $R(\lambda)$. Also, the correct geometric positioning of radiometers during the *in situ* measured R ($\lambda$) was essential.

- The OWT classification was developed for boreal region inland and coastal waters. It takes $R(\lambda)$ as input and uses key spectral features, such as the wavelength of the maximum, the slopes, and the amplitude of $R(\lambda)$, to divide water into five OWTs: Clear, Moderate, Turbid, Very Turbid, and Brown. Each OWT has different reflectance spectra which reflect different bio-optical conditions. OLCI, onboard the Sentinel-3, and MSI, onboard the Sentinel-2, can distinguish all five OWTs. Moreover, the high spatial resolution of MSI allows for monitoring the changes of OWTs by remote sensing even in smaller water bodies.

- For boreal region inland and coastal waters, using the OWT guided approach was suggested to estimate optical water quality parameters, such as the concentration of Chl-a and TSM, $a_{CDOM}(442)$, and ZSD from the $R(\lambda)$ spectra with different spectral scales, such as hyperspectral with a 1 nm step, OLCI bands, and MSI bands.

- The dominant OWT in a lake obtained from MSI and OLCI data generally agreed. However, OWTs obtained from MSI data showed more variability, while OWTs obtained from OLCI data tended to be more homogenous. The differences were caused by several factors, like the AC processor used to derive $R(\lambda)$ from satellite data, the differences in the spatial resolution of the two sensors, and the sensitivity of the OWT model due to the sensors' different spectral scales.

- The choice of an AC processor suitable for the region and sensor of interest is the first step to estimate optical water quality parameters from OLCI and MSI data. C2RCC and POLYMER AC processors were found to be the most accurate and reliable for use with OLCI images, and for MSI images, the C2RCC and C2X AC processors were most suitable. The second step is to determine the OWT for each water pixel. The third is to apply the most suitable model for each OWT to estimate optical water quality parameters.

- CDOM-rich waters which were classified into the Brown OWT need additional investigation in the future. For instance, the *in situ* measurements of $R(\lambda)$ were difficult to perform well, and $R(\lambda)$ spectra derived from the satellite sensor strongly overestimates the blue region of spectra, which can lead to misclassification of OWTs. Also, predictive models for optical water quality parameters had the lowest coefficients of determinations between 0.27–0.61.

- The OWT guided approach appeared to be suitable to provide a basis for understanding the seasonal and spatial variabilities of water bodies and can be an additional technique in water monitoring programs to improve the quality of monitoring of the optical water quality parameters.

# REFERENCES

1.  The European Parliament, the C. of the E.U. WFD Directive 2000/60/EC of the European Parliament and of the Council of 23 October 2000 establishing a framework for Community action in the field of water policy. *Off. J. Eur. Parliam.* **2000**, *327*, 1–73.

2.  Mobley, C.D. *Light and Water: Radiative Transfer in Natural Waters*; Academic Press: San Diego, CA, USA, 1994; ISBN 0-12-502750-8.

3.  Carstensen, J.; Klais, R.; Cloern, J.E. Phytoplankton blooms in estuarine and coastal waters: Seasonal patterns and key species. *Estuar. Coast. Shelf Sci.* **2015**, *162*, 98–109.

4.  Jickells, T. External inputs as a contributor to eutrophication problems. *J. Sea Res.* **2005**, *54*, 58–69.

5.  Gustafsson, B.G.; Schenk, F.; Blenckner, T.; Eilola, K.; Meier, H.E.M.; Müller-Karulis, B.; Neumann, T.; Ruoho-Airola, T.; Savchuk, O.P.; Zorita, E. Reconstructing the Development of Baltic Sea Eutrophication 1850–2006. *Ambio* **2012**, *41*, 534–548.

6.  Diaz, R.J.; Rosenberg, R. Spreading Dead Zones and Consequences for Marine Ecosystems. *Science* **2008**, *321*, 926–929.

7.  Voss, M.; Dippner, J.W.; Humborg, C.; Hürdler, J.; Korth, F.; Neumann, T.; Schernewski, G.; Venohr, M. History and scenarios of future development of Baltic Sea eutrophication. *Estuar. Coast. Shelf Sci.* **2011**, *92*, 307–322.

8.  Dickey, T.; Lewis, M.; Chang, G. Optical oceanography: Recent advances and future directions using global remote sensing and in situ observations. *Rev. Geophys.* **2006**, *44*, RG1001.

9.  Gordon, H.R.; Morel, A.Y. *Remote Assessment of Ocean Color for Interpretation of Satellite Visible Imagery: A Review*; Lecture Notes on Coastal and Estuarine Studies; American Geophysical Union: Washington, D. C., 1983; Vol. 4; ISBN 0-387-90923-0.

10. Lins, R.; Martinez, J.-M.; Motta Marques, D.; Cirilo, J.; Fragoso, C. Assessment of Chlorophyll-a Remote Sensing Algorithms in a Productive Tropical Estuarine-Lagoon System. *Remote Sens.* **2017**, *9*, 516.

11. Zimba, P. V.; Gitelson, A. Remote estimation of chlorophyll concentration in hyper-eutrophic aquatic systems: Model tuning and accuracy optimization. *Aquaculture* **2006**, *256*, 272–286.

12. Le, C.; Li, Y.; Zha, Y.; Sun, D.; Huang, C.; Lu, H. A four-band semi-analytical model for estimating chlorophyll a in highly turbid lakes: The case of Taihu Lake, China. *Remote Sens. Environ.* **2009**, *113*, 1175–1182.

13. Raag, L.; Sipelgas, L.; Uiboupin, R. Analysis of natural background and dredging-induced changes in TSM concentration from MERIS images near commercial harbours in the Estonian coastal sea. *Int. J. Remote Sens.* **2014**, *35*, 6764–6780.

14. Kyryliuk, D.; Kratzer, S. Total suspended matter derived from MERIS data as indicator for coastal processes in the Baltic Sea. *Ocean Sci. Discuss.* **2016**, 1–30.

15. Pozdnyakov, D.; Grassl, H. *Colour of inland and coastal waters. A Metgodology for its interpretation*; Springer, 2003; ISBN 978-3-540-00200-0.

16. Leppäranta, M.; Myrberg, K. *Physical Oceanography of the Baltic Sea*; Springer Berlin Heidelberg: Berlin, Heidelberg, 2009; ISBN 978-3-540-79702-9.

17. Shi, W.; Zhang, Y.; Wang, M. Deriving Total Suspended Matter Concentration from the Near-Infrared-Based Inherent Optical Properties over Turbid Waters: A Case Study in Lake Taihu. *Remote Sens.* **2018**, *10*, 333.

18. Brando, V.E.; Anstee, J.M.; Wettle, M.; Dekker, A.G.; Phinn, S.R.; Roelfsema, C. A physics based retrieval and quality assessment of bathymetry from suboptimal hyperspectral data. *Remote Sens. Environ.* **2009**, *113*, 755–770.

19. Tzortziou, M.; Zeri, C.; Dimitriou, E.; Ding, Y.; Jaffé, R.; Anagnostou, E.; Pitta, E.; Mentzafou, A. Colored dissolved organic matter dynamics and anthropogenic influences in a major transboundary river and its coastal wetland. *Limnol. Oceanogr.* **2015**, *60*, 1222–1240.

20. Markager, S.; Vincent, W.F. Spectral light attenuation and the absorption of UV and blue light in natural waters. *Limnol. Oceanogr.* **2000**, *45*, 642–650.

21. Menon, H.B.; Sangekar, N.P.; Lotliker, A.A.; Vethamony, P. Dynamics of chromophoric dissolved organic matter in Mandovi and Zuari estuaries – A study through in situ and satellite data. *ISPRS J. Photogramm. Remote Sens.* **2011**, *66*, 545–552.

22. Matsuoka, A.; Hooker, S.B.; Bricaud, A.; Gentili, B.; Babin, M. Estimating absorption coefficients of colored dissolved organic matter (CDOM) using a semi-analytical algorithm for southern Beaufort Sea waters: application to deriving concentrations of dissolved organic carbon from space. *Biogeosciences* **2013**, *10*, 917–927.

23. Copernicus. Available online: www.copernicus.eu (accessed on Mar 19, 2020).

24. ESA Sentinel Online. Available online: https://sentinel.esa.int/web/sentinel/user-guides/sentinel-2-msi (accessed on Jan 27, 2020).

25. Toming, K.; Kutser, T.; Laas, A.; Sepp, M.; Paavel, B.; Nõges, T. First Experiences in Mapping Lake Water Quality Parameters with Sentinel-2 MSI Imagery. *Remote Sens.* **2016**, *8*, 640.

26. Dogliotti, A.; Gossn, J.; Vanhellemont, Q.; Ruddick, K. Detecting and Quantifying a Massive Invasion of Floating Aquatic Plants in the Río de la Plata Turbid Waters Using High Spatial Resolution Ocean Color Imagery. *Remote Sens.* **2018**, *10*, 1140.

27. Soriano-González, J.; Angelats, E.; Fernández-Tejedor, M.; Diogene, J.; Alcaraz, C. First Results of Phytoplankton Spatial Dynamics in Two NW-Mediterranean Bays from Chlorophyll-a Estimates Using Sentinel 2: Potential Implications for Aquaculture. *Remote Sens.* **2019**, *11*, 1756.

28. ESA Sentinel Online. Available online: https://sentinel.esa.int/web/sentinel/user-guides/sentinel-3-olci (accessed on Jan 27, 2020).

29. Globolakes. Global Observatory of Lake Responses to Environmental Change. Available online: www.globolakes.ac.uk (accessed on Mar 19, 2020).

30. Verpoorter, C.; Kutser, T.; Seekell, D.A.; Tranvik, L.J. A global inventory of lakes based on high-resolution satellite imagery. *Geophys. Res. Lett.* **2014**, *41*, 6396–6402.

31. Toming, K.; Kutser, T.; Uiboupin, R.; Arikas, A.; Vahter, K.; Paavel, B. Mapping Water Quality Parameters with Sentinel-3 Ocean and Land Colour Instrument imagery in the Baltic Sea. *Remote Sens.* **2017**, *9*, 1070.

32. Caballero, I.; Stumpf, R.; Meredith, A. Preliminary Assessment of Turbidity and Chlorophyll Impact on Bathymetry Derived from Sentinel-2A and Sentinel-3A Satellites in South Florida. *Remote Sens.* **2019**, *11*, 645.

33. Ruescas, A.B.; Hieronymi, M.; Mateo-Garcia, G.; Koponen, S.; Kallio, K.; Camps-Valls, G. Machine learning regression approaches for colored dissolved organic matter (CDOM) retrieval with S2-MSI and S3-OLCI simulated data. *Remote Sens.* **2018**, *10*, 1–25.

34. Poddar, S.; Chacko, N.; Swain, D. Estimation of Chlorophyll-a in Northern Coastal Bay of Bengal Using Landsat-8 OLI and Sentinel-2 MSI Sensors. *Front. Mar. Sci.* **2019**, *6*, 598.

35. Ligi, M.; Kutser, T.; Kallio, K.; Attila, J.; Koponen, S.; Paavel, B.; Soomets, T.; Reinart, A. Testing the performance of empirical remote sensing algorithms in the Baltic Sea waters with modelled and in situ reflectance data. *Oceanologia* **2017**, *59*, 57–68.

36. Ohde, T.; Siegel, H.; Gerth, M. Validation of MERIS Level-2 products in the Baltic Sea, the Namibian coastal area and the Atlantic Ocean. *Int. J. Remote Sens.* **2007**, *28*, 609–624.

37. Harvey, T. Bio-optics, satellite remote sensing and Baltic Sea ecosystems: Applications for monitoring and management, Stockholm University, 2015.

38. Grendaitė, D.; Stonevičius, E.; Karosienė, J.; Savadova, K.; Kasperovičienė, J. Chlorophyll-a concentration retrieval in eutrophic lakes in Lithuania from Sentinel-2 data. *Geol. Geogr.* **2018**, *4*, 15–28.

39. Morel, A.; Prieur, L. Analysis of variations in ocean color. *Limnol. Oceanogr.* **1977**, *22*, 709–722.

40. Jerlov, N.G. Classification of sea water in terms of quanta irradiance. *ICES J. Mar. Sci.* **1977**.

41. Reinart, A.; Herlevi, A.; Arst, H.; Sipelgas, L. Preliminary optical classification of lakes and coastal waters in Estonia and south Finland. *J. Sea Res.* **2003**, *49*, 357–366.

42. McKee, D.; Cunningham, A.; Dudek, A. Optical water type discrimination and tuning remote sensing band-ratio algorithms: Application to retrieval of chlorophyll and Kd(490) in the Irish and Celtic Seas. *Estuar. Coast. Shelf Sci.* **2007**, *73*, 827–834.

43. Naumann, E. The Scope and Chief Problems of Regional Limnology. *Int. Rev. der gesamten Hydrobiol. und Hydrogr.* **1929**, *22*, 423–444.

44. Wernand, M.R.; Hommersom, A.; van der Woerd, H.J. MERIS-based ocean colour classification with the discrete Forel–Ule scale. *Ocean Sci.* **2013**, *9*, 477–487.

45. Moore, T.S.; Campbell, J.W.; Dowell, M.D. A class-based approach to characterizing and mapping the uncertainty of the MODIS ocean chlorophyll product. *Remote Sens. Environ.* **2009**, *113*, 2424–2430.

46. Eleveld, M.A.; Ruescas, A.B.; Hommersom, A.; Moore, T.S.; Peters, S.W.M.; Brockmann, C. An optical classification tool for global lake waters. *Remote Sens.* **2017**, *9*, 1–24.

47. Spyrakos, E.; O'Donnell, R.; Hunter, P.D.; Miller, C.; Scott, M.; Simis, S.G.H.; Neil, C.; Barbosa, C.C.F.; Binding, C.E.; Bradt, S.; et al. Optical types of inland and coastal waters. *Limnol. Oceanogr.* **2018**, *63*, 846–870.

48. Vantrepotte, V.; Loisel, H.; Dessailly, D.; Mériaux, X. Optical classification of contrasted coastal waters. *Remote Sens. Environ.* **2012**, *123*, 306–323.

49. Shi, K.; Li, Y.; Li, L.; Lu, H.; Song, K.; Liu, Z.; Xu, Y.; Li, Z. Remote chlorophyll-a estimates for inland waters based on a cluster-based classification. *Sci. Total Environ.* **2013**, *444*, 1–15.

50. Martin Traykovski, L. V.; Sosik, H.M. Feature-based classification of optical water types in the Northwest Atlantic based on satellite ocean color data. *J. Geophys. Res.* **2003**, *108*, 3150.

51. Jackson, T.; Sathyendranath, S.; Mélin, F. An improved optical classification scheme for the Ocean Colour Essential Climate Variable and its applications. *Remote Sens. Environ.* **2017**, *203*, 152–161.

52. Shen, Q.; Li, J.; Zhang, F.; Sun, X.; Li, J.; Li, W.; Zhang, B. Classification of Several Optically Complex Waters in China Using in Situ Remote Sensing Reflectance. *Remote Sens.* **2015**, *7*, 14731–14756.

53. Gordon, H.R.; Brown, O.B.; Evans, R.H.; Brown, J.W.; Smith, R.C.; Baker, K.S.; Clark, D.K. A semianalytic radiance model of ocean color. *J. Geophys. Res.* **1988**, *93*, 10909.

54. Uiboupin, R.; Laanemets, J. Upwelling characteristics derived from satellite sea surface temperature data in the Gulf of Finland, Baltic sea. *Boreal Environ. Res.* **2009**, *14*, 297–304.

55. Zhurbas, V.; Laanemets, J.; Vantera, E. Modeling of the mesoscale structure of coupled upwelling/downwelling events and the related input of nutrients to the upper mixed layer in the Gulf of Finland, baltic sea. *J. Geophys. Res. Ocean.* **2008**, *113*, 1–8.

56. Hommersom, A.; Peters, S.; Wernand, M.R.; de Boer, J. Spatial and temporal variability in bio-optical properties of the Wadden Sea. *Estuar. Coast. Shelf Sci.* **2009**, *83*, 360–370.

57. Tilstone, G.H.; Moore, G.F.; Doerffer, R.; Røttgers, R.; Ruddick, K.G.; Pasterkamp, R.; Jørgensen, P. V Regional Validation of MERIS Chlorophyll products in North Sea coastal waters. REVAMP Protocols. In Proceedings of the Working meeting on MERIS and AATSR Calibration and Geophysical Validation (ENVISAT MAVT-2003); Frascati, Italy, 2003.

58. Vabson, V.; Ansko, I.; Alikas, K.; Kuusk, J.; Vendt, R.; Reinat, A. Improving Comparability of Radiometric In Situ Measurements with Sentinel-3A/OLCI Data. In Proceedings of the the Fourth S3VT Meeting, 13–15 March 2018; Darmstadt, Germany, 2018.

59. Vabson, V.; Kuusk, J.; Ansko, I.; Vendt, R.; Alikas, K.; Ruddick, K.; Ansper, A.; Bresciani, M.; Burmester, H.; Costa, M.; et al. Laboratory Intercomparison of Radiometers Used for Satellite Validation in the 400–900 nm Range. *Remote Sens.* **2019**, *11*, 1101.

60. Ruddick, K.G.; De Cauwer, V.; Park, Y.J.; Moore, G. Seaborne measurements of near infrared water-leaving reflectance: The similarity spectrum for turbid waters. *Limnol. Oceanogr.* **2006**.

61. R. Available online: https://www.r-project.org/ (accessed on Mar 23, 2020).

62. OLCI SRFs. Available online: https://sentinel.esa.int/web/sentinel/technical-guides/sentinel-3-olci/olci-instrument/spectral-response-function-data (accessed on Jul 24, 2019).

63. MSI SRFs. Available online: https://earth.esa.int/web/sentinel/user-guides/sentinel-2-msi/document-library/-/asset_publisher/Wk0TKajiISaR/content/sentinel-2a-spectral-responses (accessed on Jul 24, 2019).

64. The International Organization for Standardization ISO 5667-3:2018 Water quality — Sampling — Part 3: Preservation and handling of water samples. **2018**, 52.

65. The International Organization for Standardization ISO 10260:1992 Water quality — Measurement of biochemical parameters — Spectrometric determination of the chlorophyll-a concentration. **1992**, 6.

66. Jeffrey, S.W.; Humphrey, G.F. New spectrophotometric equations for determining chlorophylls a, b, c1 and c2 in higher plants, algae and natural phytoplankton. *Biochem. und Physiol. der Pflanz.* **1975**, *167*, 191–194.

67. Lorenzen, C.J. Determination of Chlorophyll and Pheo-pigments: Spectrophotometric Equations. *Limnol. Oceanogr.* **1967**, *12*, 343–346.

68. Lindell, T.; Pierson, D.; Premazzi, G.; Zilioti, E. *Manual for monitoring European lakes using remote sensing techniques*; 1999; ISBN 928285390X.

69. C2RCC Processor. Available online: https://www.brockmann-consult.de/portfolio/water-quality-from-space/ (accessed on Mar 23, 2020).

70. Brockmann, C.; Doerffer, R.; Peters, M.; Stelzer, K.; Embacher, S.; Ruescas, A. Evolution of the C2RCC neural network for Sentinel 2 and 3 for the retrieval of ocean colour products in normal and extreme optically complex waters. In Proceedings of the European Space Agency, (Special Publication) ESA SP; 2016.

71. HYGEOS—Polymer. Available online: https://www.hygeos.com/polymer (accessed on Mar 23, 2020).

72. ACOLITE: Atmospheric Correction for Aquatic Applications of Landsat and Sentinel-2. Available online: https://github.com/acolite/acolite (accessed on Mar 23, 2020).

73. Sen2Cor|STEP. Available online: https://step.esa.int/main/third-party-plugins-2/sen2cor/ (accessed on Mar 23, 2020).

74. Homayouni, S.; Roux, M. Hyperspectral image analysis for material mapping using spectral matching. *Int. Arch. Photogramm. Remote Sens. Spat. Inf. Sci. - ISPRS Arch.* **2004**, 49–54.

75. Morio, J. Global and local sensitivity analysis methods for a physical system. *Eur. J. Phys.* **2011**, *32*, 1577–1583.

76. Kuhn, M.; Johnson, K. *Applied Predictive Modeling*; 1st ed.; Springer New York: New York, NY, 2013; ISBN 978-1-4614-6848-6.

77. The caret package. Available online: http://topepo.github.io/caret/index.html (accessed on Jan 21, 2020).

78. Lee, Z.; Carder, K.L.; Arnone, R.A. Deriving inherent optical properties from water color: a multiband quasi-analytical algorithm for optically deep waters. *Appl. Opt.* **2002**, *41*, 5755.

79. Vanhellemont, Q.; Ruddick, K. Advantages of high quality SWIR bands for ocean colour processing: Examples from Landsat-8. *Remote Sens. Environ.* **2015**, *161*, 89–106.

80. Fan, Y.; Li, W.; Gatebe, C.K.; Jamet, C.; Zibordi, G.; Schroeder, T.; Stamnes, K. Atmospheric correction over coastal waters using multilayer neural networks. *Remote Sens. Environ.* **2017**, *199*, 218–240.

81. Harmel, T.; Chami, M.; Tormos, T.; Reynaud, N.; Danis, P.-A. Sunglint correction of the Multi-Spectral Instrument (MSI)-SENTINEL-2 imagery over inland and sea waters from SWIR bands. *Remote Sens. Environ.* **2018**, *204*, 308–321.

82. Martins, V.; Barbosa, C.; de Carvalho, L.; Jorge, D.; Lobo, F.; Novo, E. Assessment of Atmospheric Correction Methods for Sentinel-2 MSI Images Applied to Amazon Floodplain Lakes. *Remote Sens.* **2017**, *9*, 322.

83. De Keukelaere, L.; Sterckx, S.; Adriaensen, S.; Knaeps, E.; Reusen, I.; Giardino, C.; Bresciani, M.; Hunter, P.; Neil, C.; Van der Zande, D.; et al. Atmospheric

correction of Landsat-8/OLI and Sentinel-2/MSI data using iCOR algorithm: validation for coastal and inland waters. *Eur. J. Remote Sens.* **2018**, *51*, 525–542.

84. Vabson, V.; Kuusk, J.; Ansko, I.; Vendt, R.; Alikas, K.; Ruddick, K.; Ansper, A.; Bresciani, M.; Burmester, H.; Costa, M.; et al. Field Intercomparison of Radiometers Used for Satellite Validation in the 400–900 nm Range. *Remote Sens.* **2019**, *11*, 1129.

85. Ammenberg, P.; Flink, P.; Lindell, T.; Pierson, D.; Strömbeck, N. Bio-optical modelling combined with remote sensing to assess water quality. *Int. J. Remote Sens.* **2002**, *23*, 1621–1638.

86. Flink, P.; Lindell, L.T.; Östlund, C. Statistical analysis of hyperspectral data from two Swedish lakes. *Sci. Total Environ.* **2001**, *268*, 155–169.

87. Duan, H.; Zhang, Y.; Zhang, B.; Song, K.; Wang, Z. Assessment of Chlorophyll-a Concentration and Trophic State for Lake Chagan Using Landsat TM and Field Spectral Data. *Environ. Monit. Assess.* **2007**, *129*, 295–308.

88. Dierberg, F.E.; Carriker, N.E. Field testing two instruments for remotely sensing water quality in the Tennessee Valley. *Environ. Sci. Technol.* **1994**, *28*, 16–25.

89. Gons, H.J. Optical Teledetection of Chlorophyll *a* in Turbid Inland Waters. *Environ. Sci. Technol.* **1999**, *33*, 1127–1132.

90. Koponen, S.; Attila, J.; Pulliainen, J.; Kallio, K.; Pyhälahti, T.; Lindfors, A.; Rasmus, K.; Hallikainen, M. A case study of airborne and satellite remote sensing of a spring bloom event in the Gulf of Finland. *Cont. Shelf Res.* **2007**, *27*, 228–244.

91. Moses, W.J.; Gitelson, A.A.; Berdnikov, S.; Povazhnyy, V. Estimation of chlorophyll- a concentration in case II waters using MODIS and MERIS data—successes and challenges. *Environ. Res. Lett.* **2009**, *4*, 045005.

92. Kutser, T.; Kallio, K.; Eloheimo, K.; Hannonen, T.; Pyhälahti, T.; Koponen, S.; Pulliainen, J. Quantitative monitoring of water properties with the airborne imaging spectrometer AISA. *Proc. Est. Acad. Sci. Biol. Ecol.* **1999**, *48*, 25–36.

93. Gower, J.F.R.; Doerffer, R.; Borstad, G.A. Interpretation of the 685nm peak in water-leaving radiance spectra in terms of fluorescence, absorption and scattering, and its observation by MERIS. *Int. J. Remote Sens.* **1999**, *20*, 1771–1786.

94. Zhou, L. Remote Sensing Retrieval of Chlorophyll-a Concentration in Lake Waters, Chinese Academy of Sciences, 2011.

95. Gower, J.; King, S.; Goncalves, P. Global monitoring of plankton blooms using MERIS MCI. *Int. J. Remote Sens.* **2008**, *29*, 6209–6216.

96. Gitelson, A. The peak near 700 nm on radiance spectra of algae and water: relationships of its magnitude and position with chlorophyll concentration. *Int. J. Remote Sens.* **1992**, *13*, 3367–3373.

97. Mishra, S.; Mishra, D.R. Normalized difference chlorophyll index: A novel model for remote estimation of chlorophyll-a concentration in turbid productive waters. *Remote Sens. Environ.* **2012**, *117*, 394–406.

98. Gitelson, A.A.; Gurlin, D.; Moses, W.J.; Barrow, T. A bio-optical algorithm for the remote estimation of the chlorophyll- a concentration in case 2 waters. *Environ. Res. Lett.* **2009**, *4*, 045003.

99. Kutser, T.; Paavel, B.; Verpoorter, C.; Ligi, M.; Soomets, T.; Toming, K.; Casal, G. Remote Sensing of Black Lakes and Using 810 nm Reflectance Peak for Retrieving Water Quality Parameters of Optically Complex Waters. *Remote Sens.* **2016**, *8*, 497.

100. Doxaran, D.; Froidefond, J.-M.; Castaing, P. Remote-sensing reflectance of turbid sediment-dominated waters Reduction of sediment type variations and changing illumination conditions effects by use of reflectance ratios. *Appl. Opt.* **2003**, *42*, 2623.

101. Doxaran, D.; Cherukuru, R.C.N.; Lavender, S.J. Use of reflectance band ratios to estimate suspended and dissolved matter concentrations in estuarine waters. *Int. J. Remote Sens.* **2005**, *26*, 1763–1769.

102. Matthews, M.W. A current review of empirical procedures of remote sensing in inland and near-coastal transitional waters. *Int. J. Remote Sens.* **2011**, *32*, 6855–6899.

103. Zhang, M.; Tang, J.; Dong, Q.; Song, Q.T.; Ding, J. Retrieval of total suspended matter concentration in the Yellow and East China Seas from MODIS imagery. *Remote Sens. Environ.* **2010**, *114*, 392–403.

104. Tassan, S. An improved in-water algorithm for the determination of chlorophyll and suspended sediment concentration from thematic mapper data in coastal waters. *Int. J. Remote Sens.* **1993**, *14*, 122–1229.

105. Ouillon, S.; Douillet, P.; Petrenko, A.; Neveux, J.; Dupouy, C.; Froidefond, J.M.; Andréfouët, S.; Muñoz-Caravaca, A. Optical algorithms at satellite wavelengths for total suspended matter in tropical coastal waters. *Sensors* **2008**, *8*, 4165–4185.

106. Molkov, A.A.; Fedorov, S. V.; Pelevin, V. V.; Korchemkina, E.N. Regional Models for High-Resolution Retrieval of Chlorophyll a and TSM Concentrations in the Gorky Reservoir by Sentinel-2 Imagery. *Remote Sens.* **2019**, *11*, 1215.

107. Kutser, T.; Pierson, D.C.; Kallio, K.Y.; Reinart, A.; Sobek, S. Mapping lake CDOM by satellite remote sensing. *Remote Sens. Environ.* **2005**, *94*, 535–540.

108. Menken, K.D.; Brezonik, P.L.; Bauer, M.E. Influence of chlorophyll and colored dissolved organic matter (CDOM) on lake reflectance spectra: Implications for measuring lake properties by remote sensing. *Lake Reserv. Manag.* **2006**, *22*, 179–190.

109. Kallio, K.; Attila, J.; Härmä, P.; Koponen, S.; Pulliainen, J.; Hyytiäinen, U.M.; Pyhälahti, T. Landsat ETM+ images in the estimation of seasonal lake water quality in boreal river basins. *Environ. Manage.* **2008**, *42*, 511–522.

110. Ficek, D.; Zapadka, T.; Dera, J. Remote sensing reflectance of Pomeranian lakes and the Baltic. *Oceanologia* **2011**, *53*, 959–970.

111. Brezonik, P.L.; Olmanson, L.G.; Finlay, J.C.; Bauer, M.E. Factors affecting the measurement of CDOM by remote sensing of optically complex inland waters. *Remote Sens. Environ.* **2015**, *157*, 199–215.

112. Brezonik, P.; Menken, K.D.; Bauer, M. Landsat-based remote sensing of lake water quality characteristics, including chlorophyll and colored dissolved organic matter (CDOM). *Lake Reserv. Manag.* **2005**, *21*, 373–382.

113. Griffin, C.G.; Frey, K.E.; Rogan, J.; Holmes, R.M. Spatial and interannual variability of dissolved organic matter in the Kolyma River, East Siberia, observed using satellite imagery. *J. Geophys. Res.* **2011**, *116*, G03018.

114. Kloiber, S.M.; Brezonik, P.L.; Bauer, M.E. Application of Landsat imagery to regional-scale assessments of lake clarity. *Water Res.* **2002**, *36*, 4330–4340.

115. Olmanson, L.G.; Bauer, M.E.; Brezonik, P.L. A 20-year Landsat water clarity census of Minnesota's 10,000 lakes. *Remote Sens. Environ.* **2008**, *112*, 4086–4097.

116. Wu, M.; Zhang, W.; Wang, X.; Luo, D. Application of MODIS satellite data in monitoring water quality parameters of Chaohu Lake in China. *Environ. Monit. Assess.* **2009**, *148*, 255–264.

117. Hellweger, F.L.; Schlosser, P.; Lall, U.; Weissel, J.K. Use of satellite imagery for water quality studies in New York Harbor. *Estuar. Coast. Shelf Sci.* **2004**, *61*, 437–448.

118. LEGMC (State Limited Liability Company "Latvian Environment, Geology and Meteorology Centre") National Monitoring Database. Available online: http://www.meteo.lv/lapas/noverojumi/virszemes-udens/virszemes-udens_ievads?id=1369&nid=477 (accessed on Mar 8, 2020).

119. Arst, H. *Optical properties and remote sensing of multicomponental water bodies*; Springer, 2003; ISBN 978-3-540-00629-9.

120. Bilaletdin, Ä.; Frisk, T.; Kaipainen, H. An integrated modelling system for the water protection project of Lake Burtnieks. *SIL Proceedings, 1922-2010* **2006**, *29*, 1399–1403.

121. Nõges, P.; Tuvikene, L. Spatial and annual variability of environmental and phytoplankton indicators in Lake Võrtsjärv: implications for water quality monitoring. *Est. J. Ecol.* **2012**, *61*, 227.

122. Raukas, A. Bottom deposits. In *Lake Võrtsjärv*; Haberman, J., Pihu, E., Raukas, A., Eds.; Estonian Encyclopedia Publishers: Tallinn, Estonia, 2004; pp. 79–86.

123. LEGMC (State Limited Liability Company "Latvian Environment, Geology and Meteorology Centre"), Assessment on Data Availability and Quality. Available online: www.meteo.lv/fs/CKFinderJava/userfiles/files/Par_centru/ES_projekti/Projekts_Udens_kvalitate/Assessment_on_data_availability_and_quality.doc (accessed on Mar 19, 2020).

124. Keskkonnaministeerium (Ministry of the Environment), Water Monitoring Program 2016–2021. Available online: http://www.envir.ee/et/eesmargid-tegevused/vesi/vesikondade-veeseireprogramm-2016-2021 (accessed on Mar 19, 2020).

# SUMMARY IN ESTONIAN

## Optiliste veetüüpide põhine lähenemine
## sise- ja rannikuvee veekvaliteedi hindamiseks

Inimestele on meeldinud ajast aega elada seal, kus maa ja vesi kohtuvad. Veekogud on vajalikud nii põllumajanduse, majapidamise kui ka tööstuse veevarustuseks, bioloogilise mitmekesisuse toetamiseks ning kalapüügi- ja puhkamisvõimalusteks. Suurenenud inimtegevuse mõju on põhjustanud veekogude seisundi muutumist. Seisundi pidev jälgimine aitab kaardistada olukorda, hinnata inimtegevuse mõju ulatust ja vajadust reageerida. Pikaajalised veeseireprogrammid põhinevad suurel hulgal *in situ* punktmõõtmistel. See meetod ei suuda kajastada kogu veekogu kiiresti muutuvaid omadusi ja reaalselt seisundit. Seetõttu on oluline lisaks rakendada veekeskkonna operatiivse jälgimise meetodeid, milles kaugseire on üks võimsamaid.

Kaugseire pakub tõhusaid viise veekvaliteedi ruumiliste ja ajaliste erinevuste jälgimiseks. Euroopa Liidu ja Euroopa Kosmoseagentuuri Coperniⅽuse programmi raames on loodud Sentinel seeria satelliidid. Praegu on toimimas kaks Maa vaatlusmissiooni, mis sobivad sise- ja rannikuvee optiliste omaduste jälgimiseks. Sentinel-3 seeria satelliitide pardal on keskmise ruumilise lahutusvõime (300 m) ja 21 spektraalkanaliga sensor OLCI. OLCI kanalite asukohad on valitud veevärvuse mõõtmiseks, aga tema ruumiline lahutusvõime lubab seirata umbes 1000 suurimat järve maailma 117 miljonist järvest. Sentinel-2 seeria satelliitide pardal oleval sensoril MSI on 13 spektraalkanalit ja oluliselt kõrgem ruumiline lahutusvõime (10, 20 ja 60 m), mis võimaldab väiksemate veekogude ja erinevate nähtuste (nt bioloogilise aktiivsuse filamentide ja keeriste) üksikasjalikumat uurimist.

Coperniⅽuse programmi suure spektraalse, ruumilise ja ajalise lahutusvõimega andmete tasuta kättesaadavus ning plaanitud edasine järjepidevus vähemalt paarikümne aasta jooksul on tekitanud huvi kasutada kaugseire võimalusi sise- ja rannikuvete veekvaliteedi jälgimiseks. Need veed on optiliselt keerukad, kuna vee optilised omadused on mõjutatud erinevate optiliselt aktiivsete ainete (värvunud lahustunud orgaaniline aine (CDOM), klorofüll ja heljum) poolt sõltumatult. Seetõttu on optiliselt keerukate vete kaugseire komplitseeritum ja standardsed kaugseire tulemid sageli ei tööta neis vetes. Vee klassifitseerimine võib olla võtmelahendus optiliselt keerukate veekogude funktsionaalsete kaugseire algoritmide väljatöötamiseks. Klassifikatsioone kasutatakse laialdaselt maastiku kaugseires ja selle meetodi rakendamine on ka vee kaugseires viimastel aastatel kasvanud. Siiski on raske leida optiliste veetüüpide klassifikatsiooni, mis sobiks boreaalse piirkonna sise- ja rannikuvetele.

Doktoritöö peaeesmärgiks oli arendada kaugseire andmetel põhinevat boreaalse piirkonna sise- ja rannikuvete veekvaliteedi hindamismetoodikat. Konkreetsemateks eesmärkideks olid (1) uurida mõõtmiskeskkonna mõju *in situ* mõõdetud vee peegeldumisspektri varieeruvusele; (2) arendada optiliste veetüüpide klassifikatsioon, mida saaks rakendada nii OLCI kui ka MSI andmetele;

(3) töötada välja lahendus veekvaliteedi optiliste parameetrite (klorofüll a, heljum, CDOM ja Secchi ketta sügavus) hindamiseks peegeldumisspektritest; (4) võrrelda OLCI ja MSI andmetest tuletatud optiliste veetüüpide võrreldavust; ja (5) leida kõige sobivamad OLCI ja MSI andmete töötlemise sammud.

Boreaalse piirkonna sise- ja rannikuvete jaoks loodi optiliste veetüüpide klassifikatsioon, mis põhineb vee peegeldumisspektril ja jaotab veed viide optilisse veetüüpi: Selge, Mõõdukas, Sogane, Väga sogane ja Pruun. Loodud klassifikatsioon on rakendatav nii OLCI kui ka MSI andmetele. Tänu MSI kõrgele ruumilisele lahutusvõimele on võimalik jälgida optiliste veetüüpide muutust nüüd ka väiksemates veekogudes.

Klassifikatsiooni aluseks oleva parameetri – peegeldumisspektri – mõõtmise kvaliteedil on oluline roll tulemusele. Leiti, et *in situ* mõõdetud peegeldumisspektri määramatused olid madalamad vahemikus 500–700 nm. Seejuures mõõtmiskeskkonna tingimused, nagu laine kõrgus, tuule kiirus ja muutuvad valgustingimused, olid olulised parameetrid, mis mõjutasid peegeldumisspektri mõõtemääramatuse suurenemise tõenäosust.

Kaugseire andmetest veekvaliteedi optiliste parameetrite – klorofüll a, heljumi, CDOM'i ja Secchi ketta sügavuse – hindamiseks soovitati kasutada optiliste veetüüpide põhist lähenemist, kus iga parameetri jaoks leiti igale optilisele veetüübile kõige sobilikum algoritm kaugseire andmete interpreteerimiseks.

OLCI ja MSI andmetest tuletatud järved domineerivad optilised veetüübid olid omavahel kooskõlas. MSI andmetest saadud optilised veetüübid näitasid suuremat varieeruvust kui OLCI andmetest määratud veetüübid. Erinevused olid põhjustatud näiteks atmosfääri korrektsiooni protsessorist, mida kasutati satelliidi andmetest peegeldumisspektri tuletamiseks, OLCI ja MSI erinevast ruumilisest lahutusvõimest ning optiliste veetüüpide klassifikatsiooni tundlikkusest erinevatel sensoritel.

Veekvaliteedi optiliste parameetrite hindamise esimeseks sammuks OLCI ja MSI andmetest oli piirkonna ja sensori jaoks sobiliku atmosfääri korrektsiooni protsessori valimine. Leiti, et atmosfääri korrektsiooni protsessorid C2RCC ja POLYMER olid kõige täpsemad ja usaldusväärsemad OLCI andmetele ning C2RCC ja C2X sensori MSI andmetele. Teise sammuna määrati optiline veetüüp igale veepikslile. Lõpuks rakendati veekvaliteedi optiliste parameetrite hindamiseks optiliste veetüüpide põhiseid algoritme.

CDOM-rikkad veed, mis klassifitseeriti Pruuni optilisse veetüüpi, vajavad tulevikus täiendavat uurimist, sest nende veekvaliteedi optiliste parameetrite algoritmidel olid madalad determinatsioonikordajad (vahemikus 0.27–0.61). Lisaks leiti, et satelliidi andmetest tuletatud vee peegeldumisspektrid tihti spektri sinises osas olid tugevalt ülehinnatud, mis võib põhjustada spektrite valesti klassifitseerimist Selgesse optilisse veetüüpi.

Käesoleva töö peamine väärtus seisneb automatiseeritud algoritmi väljaarendamises, mis võimaldab algatada Eesti ja meie lähipiirkonna veekogude kaugseire integreerimist operatiivsesse seiresse.

# ACKNOWLEDGEMENTS

have made me want to not to miss your life, so to be with you, I have developed pretty good time-planning skills; however, sometimes I find that sleep is overrated. Erko, my brother, I appreciate that even though we do not see each other often enough, you take the time to call. You are the master who understands the fine line between when to ask about my studies and when to stop asking when I will finish. Kiku, you are my long-awaited friend who is always ready to go with me for a walk in the woods to clear my head, regardless of the weather. Tiia, Toomas, Tiina, and Tuuli, I am thankful for your understanding and support. And Riina and Uno, my parents, I appreciate your never-ending support and that you raised me with an attitude to never give up. Thirteen years of doctoral studies are not easy, but I made it.

# PUBLICATIONS

# CURRICULUM VITAE

**Name:** Kristi Uudeberg
**Date of birth:** September 8$^{th}$, 1983
**Contact:** kristi.uudeberg@ut.ee

**Education:**
2007–2020   University of Tartu, PhD studies in physics
2005–2007   University of Tartu, MSc in applied physics
2002–2005   University of Tartu, BSc in physics
1999–2002   Nõo Real Gymnasium, high school
1990–1999   Põltsamaa Co-educational Gymnasium, primary school

**Employment:**
2018–         Tartu Observatory (University of Tartu), junior researcher
2016–2017   Tartu Observatory, junior researcher
2007–2016   Cybernetica AS, systems analyst
2006–2007   Cybernetica AS, software tester
2005–2016   Tartu Observatory, engineer

**Scientific activity**
 **Awards**
- Winner of Copernicus OceanHack, 22.–24.11.2019, Estonia. Team IceWise.
- Gerda Spohr Scholarship, 2017
- Best poster award, HIGHROC Science Conference 2017, Brussel. Poster: Uudeberg, K., Põru, G., Ansko, I., Ansper, A., Ligi, M., "Estimation of the lakes optical water types from satellites' images".
- Outstanding Student Presentation Awards, Ocean Scienas Meeting 2008, Florida. Poster: Valdmets, K., Ansko, I., Reinart, A., "Effect of Calibration Uncertainty and Spectral Band Location to Modeled Remote Sensing Reflectance".

 **Additional courses**
- Introduction to ecological modelling, Tartu, Estonia, 29.10–02.11.2018
- 9th ESA Earth Observation Summer School, Frascati, Italy, 30.07.–10.08.2018
- Coastal Altimetry Training, Frascati, Italy, 12.06.2018
- AIT Summer School – Sentinel for water resources, Sirmione, Italy, 18.–22.09.2017
- NordForsk PhD Training Course "Remote Sensing of the Baltic Sea and Other Optically Complex Waters", Lauenburg, Germany, 28.10.–01.11. 2012
- Pleasure Craft Operator Training, Tartu Kalevi Jahtklubi, Estonia, 24.03.–30.04.2012
- ESA Radar Remote Sensing Course, Tartu, Estonia, 16.–20.04.2012

- Radiative transfer theory and practice of Hydrolight software, Stockholm University, Sweden, 15.–21.05.2011
- Physical Oceanography of the Baltic Sea, University of Helsinki, Finland, 11.06.–16.06.2009

**Supervised B.Sc. theses**
- Getter Põru, "Classifying water types from satellite data using multinomia logistic model", supervisor: E. Käärik, K. Uudeberg, 2018
- Kerttu-Liis Kõks, "Optical water type guided approach for lakes suspended matter algorithms", supervisor: K. Uudeberg, 2018
- Evelin Kangro, "Validation of MERIS/Envisat water quality products on Estonian lakes", supervisors: A. Reinart, K. Uudeberg, 2012
- Elar Asuküll, "Methods for determing water color", supervisors: A. Reinart, K. Uudeberg, 2009

**Publications**

**Uudeberg, K.**; Aavaste, A.; Kõks, K.-L.; Ansper, A.; Uusõue, M.; Kangro, K.; Ansko, I.; Ligi, M.; Toming, K.; Reinart, A. Optical Water Type Guided Approach to Estimate Optical Water Quality Parameters. *Remote Sens.* 2020, 12, 931.

Alikas, K.; Ansko, I.; Vabson, V.; Ansper, A.; Kangro, K.; **Uudeberg, K.**; Ligi, M. Consistency of Radiometric Satellite Data over Lakes and Coastal Waters with Local Field Measurements. *Remote Sens.* 2020, 12, 616.

Soomets, T.; **Uudeberg, K.**; Jakovels, D.; Brauns, A.; Zagars, M.; Kutser, T. Validation and Comparison of Water Quality Products in Baltic Lakes Using Sentinel-2 MSI and Sentinel-3 OLCI Data. *Sensors* 2020, 20, 742.

Soomets, T.; **Uudeberg, K.**; Jakovels, D.; Zagars, M.; Reinart, A.; Brauns, A.; Kutser, T. Comparison of Lake Optical Water Types Derived from Sentinel-2 and Sentinel-3. Remote Sens. 2019, 11, 2883.

**Uudeberg, K.**; Ansko, I.; Põru, G.; Ansper, A.; Reinart, A. Using Optical Water Types to Monitor Changes in Optically Complex Inland and Coastal Waters. Remote Sens. 2019, 11, 2297.

Randla, M.; Ligi, M.; **Uudeberg, K.**; Kutser, T.; Bourrin, F. Variability of suspended particles properties in Pärnu Bay, Baltic Sea. In Proceedings of the Ocean Optics XXIV Conference, Dubrovnik, Croatia, 7–12 October 2018.

Randla, M.; **Uudeberg, K.**; Ligi, M.; Bourrin, F. Heljumi omaduste ja dünaamika varieerumine Pärnu lahes, *Kaugseire Eestis 2018* 2018, 41–50.

**Uudeberg, K.**; Ansko, I.; Lätt, S.; Randoja, R. An integrated collaborative tool for water remote sensing data management and analysis (at Tartu Observatory). In Proceedings of the Ocean Optics XXI Conference; Glasgow, Scotland; 8–12 October 2012.

Alikas, K.; Ansko, I.; Reinart, A.; Lill, E.; **Valdmets, K.** Testing available MERIS image processors for lakes. In Proceedings of 2nd MERIS – (A)ATSR User Workshop, Frascati, Italy, 22–26 September 2008.

Reinart, A.; **Valdmets, K.** Variability of optical water types in Lake Peipsi. *Proc. Est. Acad. Sci. Biol. Ecol.* 2007, 56, 33−46.

Reinart, A.; Ohvril, H.; Alikas, K.; Ibrus, P.; Teral, H.; **Valdmets, K.**; Okulov, O. MERIS products over large European lakes – comparison with measured data about aerosol and water quality. In Proceedings of Envisat Symposium 2007, Montreux, Switzerland, 23–27 April 2007.

# ELULOOKIRJELDUS

**Nimi:**        Kristi Uudeberg
**Sünniaeg:**    8. september 1983
**Kontakt:**     kristi.uudeberg@ut.ee

**Haridus:**
2007–2020   Tartu Ülikool, doktoriõpe füüsikas
2005–2007   Tartu Ülikool, magistriõpe rakendusfüüsikas
2002–2005   Tartu Ülikool, bakalaureuseõpe füüsikas
1999–2002   Nõo Reaalgümnaasium
1990–1999   Põltsamaa Ühisgümnaasium

**Teenistuskäik:**
2018–        Tartu Observatoorium (Tartu Ülikool), nooremteadur
2016–2017   Tartu Observatoorium, nooremteadur
2007–2016   Cybernetica AS, süsteemianalüütik
2006–2007   Cybernetica AS, tarkvara testija
2005–2016   Tartu Observatoorium, insener

**Teadustegevus**
**Tunnustused**
- Copernicus OceanHack võitja, 22.–24.11.2019, Eesti. Meeskond IceWise.
- Gerda Spohri nimeline stipendium, 2017
- Parima postri preemia, HIGHROC Science Conference 2017, Brüssel. Poster: Uudeberg, K., Põru, G., Ansko, I., Ansper, A., Ligi, M., "Estimation of the lakes optical water types from satellites' images".
- Väljapaistva esitluse tudengi preemia, Ocean Scienas Meeting 2008, Florida. Poster: Valdmets, K., Ansko, I., Reinart, A., "Effect of Calibration Uncertainty and Spectral Band Location to Modeled Remote Sensing Reflectance".

**Täiendkursused**
- Introduction to ecological modelling, Tartu, Eesti, 29.10–02.11.2018
- 9th ESA Earth Observation Summer School, Frascati, Itaalia, 30.07.–10.08.2018
- Coastal Altimetry Training, Frascati, Itaalia, 12.06.2018
- AIT Summer School – Sentinel for water resources, Sirmione, Itaalia, 18.–22.09.2017
- NordForsk PhD Training Course "Remote Sensing of the Baltic Sea and Other Optically Complex Waters", Lauenburg, Saksamaa, 28.10.–01.11. 2012
- Väikelaevajuhtide koolitus, Tartu Kalevi Jahtklubi, Eesti, 24.03.–30.04. 2012
- ESA Radar Remote Sensing Course, Tartu, Estonia, 16.–20.04.2012

- Radiative transfer theory and practice of Hydrolight software, Stockholm University, Rootsi, 15.–21.05.2011
- Physical Oceanography of the Baltic Sea, University of Helsinki, Soome, 11.06.–16.06.2009

**Juhendatud bakalaureusetööd**

- Getter Põru, "Veekogude klassifitseerimine satelliidiandmetelt multinomiaalse logistilise mudeliga", juhendajad: E. Käärik, K. Uudeberg, 2018
- Kerttu-Liis Kõks, "Järvede optilise klassifikatsiooni põhised heljumi algoritmid", juhendaja: K. Uudeberg, 2018
- Evelin Kangro, "MERIS/Envisat täislahutusega piltide järvede vee kvaliteedinäitajate valideerimine", juhendajad: A. Reinart, K. Uudeberg, 2012
- Elar Asuküll, "Vee värvuse määramise meetodid", juhendajad: A. Reinart, K. Uudeberg, 2009

**Publikatsioonid**

**Uudeberg, K.**; Aavaste, A.; Kõks, K.-L.; Ansper, A.; Uusõue, M.; Kangro, K.; Ansko, I.; Ligi, M.; Toming, K.; Reinart, A. Optical Water Type Guided Approach to Estimate Optical Water Quality Parameters. *Remote Sens.* 2020, 12, 931.

Alikas, K.; Ansko, I.; Vabson, V.; Ansper, A.; Kangro, K.; **Uudeberg, K.**; Ligi, M. Consistency of Radiometric Satellite Data over Lakes and Coastal Waters with Local Field Measurements. *Remote Sens.* 2020, 12, 616.

Soomets, T.; **Uudeberg, K.**; Jakovels, D.; Brauns, A.; Zagars, M.; Kutser, T. Validation and Comparison of Water Quality Products in Baltic Lakes Using Sentinel-2 MSI and Sentinel-3 OLCI Data. *Sensors* 2020, 20, 742.

Soomets, T.; **Uudeberg, K.**; Jakovels, D.; Zagars, M.; Reinart, A.; Brauns, A.; Kutser, T. Comparison of Lake Optical Water Types Derived from Sentinel-2 and Sentinel-3. Remote Sens. 2019, 11, 2883.

**Uudeberg, K.**; Ansko, I.; Põru, G.; Ansper, A.; Reinart, A. Using Optical Water Types to Monitor Changes in Optically Complex Inland and Coastal Waters. Remote Sens. 2019, 11, 2297.

Randla, M.; Ligi, M.; **Uudeberg, K.**; Kutser, T.; Bourrin, F. Variability of suspended particles properties in Pärnu Bay, Baltic Sea. In Proceedings of the Ocean Optics XXIV Conference, Dubrovnik, Croatia, 7–12 October 2018.

Randla, M.; **Uudeberg, K.**; Ligi, M.; Bourrin, F. Heljumi omaduste ja dünaamika varieerumine Pärnu lahes, *Kaugseire Eestis 2018* 2018, 41–50.

**Uudeberg, K.**; Ansko, I.; Lätt, S.; Randoja, R. An integrated collaborative tool for water remote sensing data management and analysis (at Tartu Observatory). In Proceedings of the Ocean Optics XXI Conference; Glasgow, Scotland; 8–12 October 2012.

Alikas, K.; Ansko, I.; Reinart, A.; Lill, E.; **Valdmets, K.** Testing available MERIS image processors for lakes. In Proceedings of 2nd MERIS – (A)ATSR User Workshop, Frascati, Italy, 22–26 September 2008.

Reinart, A.; **Valdmets, K.** Variability of optical water types in Lake Peipsi. *Proc. Est. Acad. Sci. Biol. Ecol.* 2007, 56, 33−46.

Reinart, A.; Ohvril, H.; Alikas, K.; Ibrus, P.; Teral, H.; **Valdmets, K.**; Okulov, O. MERIS products over large European lakes – comparison with measured data about aerosol and water quality. In Proceedings of Envisat Symposium 2007, Montreux, Switzerland, 23–27 April 2007.

# DISSERTATIONES PHYSICAE
# UNIVERSITATIS TARTUENSIS

1. **Andrus Ausmees.** XUV-induced electron emission and electron-phonon interaction in alkali halides. Tartu, 1991.
2. **Heiki Sõnajalg.** Shaping and recalling of light pulses by optical elements based on spectral hole burning. Tartu, 1991.
3. **Sergei Savihhin.** Ultrafast dynamics of F-centers and bound excitons from picosecond spectroscopy data. Tartu, 1991.
4. **Ergo Nõmmiste.** Leelishalogeniidide röntgenelektronemissioon kiiritamisel footonitega energiaga 70–140 eV. Tartu, 1991.
5. **Margus Rätsep.** Spectral gratings and their relaxation in some low-temperature impurity-doped glasses and crystals. Tartu, 1991.
6. **Tõnu Pullerits.** Primary energy transfer in photosynthesis. Model calculations. Tartu, 1991.
7. **Olev Saks.** Attoampri diapasoonis voolude mõõtmise füüsikalised alused. Tartu, 1991.
8. **Andres Virro.** AlGaAsSb/GaSb heterostructure injection lasers. Tartu, 1991.
9. **Hans Korge.** Investigation of negative point discharge in pure nitrogen at atmospheric pressure. Tartu, 1992.
10. **Jüri Maksimov.** Nonlinear generation of laser VUV radiation for high-resolution spectroscopy. Tartu, 1992.
11. **Mark Aizengendler.** Photostimulated transformation of aggregate defects and spectral hole burning in a neutron-irradiated sapphire. Tartu, 1992.
12. **Hele Siimon.** Atomic layer molecular beam epitaxy of $A^2B^6$ compounds described on the basis of kinetic equations model. Tartu, 1992.
13. **Tõnu Reinot.** The kinetics of polariton luminescence, energy transfer and relaxation in anthracene. Tartu, 1992.
14. **Toomas Rõõm.** Paramagnetic $H^{2-}$ and $F^+$ centers in CaO crystals: spectra, relaxation and recombination luminescence. Tallinn, 1993.
15. **Erko Jalviste.** Laser spectroscopy of some jet-cooled organic molecules. Tartu, 1993.
16. **Alvo Aabloo.** Studies of crystalline celluloses using potential energy calculations. Tartu, 1994.
17. **Peeter Paris.** Initiation of corona pulses. Tartu, 1994.
18. **Павел Рубин.** Локальные дефектные состояния в $CuO_2$ плоскостях высокотемпературных сверхпроводников. Тарту, 1994.
19. **Olavi Ollikainen.** Applications of persistent spectral hole burning in ultrafast optical neural networks, time-resolved spectroscopy and holographic interferometry. Tartu, 1996.
20. **Ülo Mets.** Methodological aspects of fluorescence correlation spectroscopy. Tartu, 1996.
21. **Mikhail Danilkin.** Interaction of intrinsic and impurity defects in CaS:Eu luminophors. Tartu, 1997.

22. **Ирина Кудрявцева.** Создание и стабилизация дефектов в кристаллах KBr, KCl, RbCl при облучении ВУФ-радиацией. Тарту, 1997.
23. **Andres Osvet.** Photochromic properties of radiation-induced defects in diamond. Tartu, 1998.
24. **Jüri Örd.** Classical and quantum aspects of geodesic multiplication. Tartu, 1998.
25. **Priit Sarv.** High resolution solid-state NMR studies of zeolites. Tartu, 1998.
26. **Сергей Долгов.** Электронные возбуждения и дефектообразование в некоторых оксидах металлов. Тарту, 1998.
27. **Kaupo Kukli.** Atomic layer deposition of artificially structured dielectric materials. Tartu, 1999.
28. **Ivo Heinmaa.** Nuclear resonance studies of local structure in $RBa_2Cu_3O_{6+x}$ compounds. Tartu, 1999.
29. **Aleksander Shelkan.** Hole states in $CuO_2$ planes of high temperature superconducting materials. Tartu, 1999.
30. **Dmitri Nevedrov.** Nonlinear effects in quantum lattices. Tartu, 1999.
31. **Rein Ruus.** Collapse of 3d (4f) orbitals in 2p (3d) excited configurations and its effect on the x-ray and electron spectra. Tartu, 1999.
32. **Valter Zazubovich.** Local relaxation in incommensurate and glassy solids studied by Spectral Hole Burning. Tartu, 1999.
33. **Indrek Reimand.** Picosecond dynamics of optical excitations in GaAs and other excitonic systems. Tartu, 2000.
34. **Vladimir Babin.** Spectroscopy of exciton states in some halide macro- and nanocrystals. Tartu, 2001.
35. **Toomas Plank.** Positive corona at combined DC and AC voltage. Tartu, 2001.
36. **Kristjan Leiger.** Pressure-induced effects in inhomogeneous spectra of doped solids. Tartu, 2002.
37. **Helle Kaasik.** Nonperturbative theory of multiphonon vibrational relaxation and nonradiative transitions. Tartu, 2002.
38. **Tõnu Laas.** Propagation of waves in curved spacetimes. Tartu, 2002.
39. **Rünno Lõhmus.** Application of novel hybrid methods in SPM studies of nanostructural materials. Tartu, 2002.
40. **Kaido Reivelt.** Optical implementation of propagation-invariant pulsed free-space wave fields. Tartu, 2003.
41. **Heiki Kasemägi.** The effect of nanoparticle additives on lithium-ion mobility in a polymer electrolyte. Tartu, 2003.
42. **Villu Repän.** Low current mode of negative corona. Tartu, 2004.
43. **Алексей Котлов.** Оксианионные диэлектрические кристаллы: зонная структура и электронные возбуждения. Tartu, 2004.
44. **Jaak Talts.** Continuous non-invasive blood pressure measurement: comparative and methodological studies of the differential servo-oscillometric method. Tartu, 2004.
45. **Margus Saal.** Studies of pre-big bang and braneworld cosmology. Tartu, 2004.

46. **Eduard Gerškevitš.** Dose to bone marrow and leukaemia risk in external beam radiotherapy of prostate cancer. Tartu, 2005.

47. **Sergey Shchemelyov.** Sum-frequency generation and multiphoton ionization in xenon under excitation by conical laser beams. Tartu, 2006.

48. **Valter Kiisk.** Optical investigation of metal-oxide thin films. Tartu, 2006.

49. **Jaan Aarik.** Atomic layer deposition of titanium, zirconium and hafnium dioxides: growth mechanisms and properties of thin films. Tartu, 2007.

50. **Astrid Rekker.** Colored-noise-controlled anomalous transport and phase transitions in complex systems. Tartu, 2007.

51. **Andres Punning.** Electromechanical characterization of ionic polymer-metal composite sensing actuators. Tartu, 2007.

52. **Indrek Jõgi.** Conduction mechanisms in thin atomic layer deposited films containing $TiO_2$. Tartu, 2007.

53. **Aleksei Krasnikov.** Luminescence and defects creation processes in lead tungstate crystals. Tartu, 2007.

54. **Küllike Rägo.** Superconducting properties of $MgB_2$ in a scenario with intra- and interband pairing channels. Tartu, 2008.

55. **Els Heinsalu.** Normal and anomalously slow diffusion under external fields. Tartu, 2008.

56. **Kuno Kooser.** Soft x-ray induced radiative and nonradiative core-hole decay processes in thin films and solids. Tartu, 2008.

57. **Vadim Boltrushko.** Theory of vibronic transitions with strong nonlinear vibronic interaction in solids. Tartu, 2008.

58. **Andi Hektor.** Neutrino Physics beyond the Standard Model. Tartu, 2008.

59. **Raavo Josepson.** Photoinduced field-assisted electron emission into gases. Tartu, 2008.

60. **Martti Pärs.** Study of spontaneous and photoinduced processes in molecular solids using high-resolution optical spectroscopy. Tartu, 2008.

61. **Kristjan Kannike.** Implications of neutrino masses. Tartu, 2008.

62. **Vigen Issahhanjan.** Hole and interstitial centres in radiation-resistant MgO single crystals. Tartu, 2008.

63. **Veera Krasnenko.** Computational modeling of fluorescent proteins. Tartu, 2008.

64. **Mait Müntel.** Detection of doubly charged higgs boson in the CMS detector. Tartu, 2008.

65. **Kalle Kepler.** Optimisation of patient doses and image quality in diagnostic radiology. Tartu, 2009.

66. **Jüri Raud.** Study of negative glow and positive column regions of capillary HF discharge. Tartu, 2009.

67. **Sven Lange.** Spectroscopic and phase-stabilisation properties of pure and rare-earth ions activated $ZrO_2$ and $HfO_2$. Tartu, 2010.

68. **Aarne Kasikov.** Optical characterization of inhomogeneous thin films. Tartu, 2010.

69. **Heli Valtna-Lukner.** Superluminally propagating localized optical pulses. Tartu, 2010.

70. **Artjom Vargunin.** Stochastic and deterministic features of ordering in the systems with a phase transition. Tartu, 2010.

71. **Hannes Liivat.** Probing new physics in e+e− annihilations into heavy particles via spin orientation effects. Tartu, 2010.

72. **Tanel Mullari.** On the second order relativistic deviation equation and its applications. Tartu, 2010.

73. **Aleksandr Lissovski.** Pulsed high-pressure discharge in argon: spectroscopic diagnostics, modeling and development. Tartu, 2010.

74. **Aile Tamm.** Atomic layer deposition of high-permittivity insulators from cyclopentadienyl-based precursors. Tartu, 2010.

75. **Janek Uin.** Electrical separation for generating standard aerosols in a wide particle size range. Tartu, 2011.

76. **Svetlana Ganina.** Hajusandmetega ülesanded kui üks võimalus füüsikaõppe efektiivsuse tõstmiseks. Tartu, 2011

77. **Joel Kuusk.** Measurement of top-of-canopy spectral reflectance of forests for developing vegetation radiative transfer models. Tartu, 2011.

78. **Raul Rammula**. Atomic layer deposition of $HfO_2$ – nucleation, growth and structure development of thin films. Tartu, 2011.

79. **Сергей Наконечный.** Исследование электронно-дырочных и интерстициал-вакансионных процессов в монокристаллах MgO и LiF методами термоактивационной спектроскопии. Тарту, 2011.

80. **Niina Voropajeva.** Elementary excitations near the boundary of a strongly correlated crystal. Tartu, 2011.

81. **Martin Timusk.** Development and characterization of hybrid electrooptical materials. Tartu, 2012, 106 p.

82. **Merle Lust.** Assessment of dose components to Estonian population. Tartu, 2012, 84 p.

83. **Karl Kruusamäe.** Deformation-dependent electrode impedance of ionic electromechanically active polymers. Tartu, 2012, 128 p.

84. **Liis Rebane.** Measurement of the $W \to \tau\nu$ cross section and a search for a doubly charged Higgs boson decaying to τ-leptons with the CMS detector. Tartu, 2012, 156 p.

85. **Jevgeni Šablonin.** Processes of structural defect creation in pure and doped MgO and NaCl single crystals under condition of low or super high density of electronic excitations. Tartu, 2013, 145 p.

86. **Riho Vendt**. Combined method for establishment and dissemination of the international temperature scale. Tartu, 2013, 108 p.

87. **Peeter Piksarv.** Spatiotemporal characterization of diffractive and non-diffractive light pulses. Tartu, 2013, 156 p.

88. **Anna Šugai.** Creation of structural defects under superhigh-dense irradiation of wide-gap metal oxides. Tartu, 2013, 108 p.

89. **Ivar Kuusik.** Soft X-ray spectroscopy of insulators. Tartu, 2013, 113 p.

90. **Viktor Vabson**. Measurement uncertainty in Estonian Standard Laboratory for Mass. Tartu, 2013, 134 p.

91. **Kaupo Voormansik.** X-band synthetic aperture radar applications for environmental monitoring. Tartu, 2014, 117 p.
92. **Deivid Pugal.** hp-FEM model of IPMC deformation. Tartu, 2014, 143 p.
93. **Siim Pikker.** Modification in the emission and spectral shape of photostable fluorophores by nanometallic structures. Tartu, 2014, 98 p.
94. **Mihkel Pajusalu**. Localized Photosynthetic Excitons. Tartu, 2014, 183 p.
95. **Taavi Vaikjärv.** Consideration of non-adiabaticity of the Pseudo-Jahn-Teller effect: contribution of phonons. Tartu, 2014, 129 p.
96. **Martin Vilbaste.** Uncertainty sources and analysis methods in realizing SI units of air humidity in Estonia. Tartu, 2014, 111 p.
97. **Mihkel Rähn.** Experimental nanophotonics: single-photon sources- and nanofiber-related studies. Tartu, 2015, 107 p.
98. **Raul Laasner.** Excited state dynamics under high excitation densities in tungstates. Tartu, 2015, 125 p.
99. **Andris Slavinskis.** EST Cube-1 attitude determination. Tartu, 2015, 104 p.
100. **Karlis Zalite**. Radar Remote Sensing for Monitoring Forest Floods and Agricultural Grasslands. Tartu, 2016, 124 p.
101. **Kaarel Piip.** Development of LIBS for *in-situ* study of ITER relevant materials. Tartu, 2016, 93 p.
102. **Kadri Isakar.** $^{210}$Pb in Estonian air: long term study of activity concentrations and origin of radioactive lead. Tartu, 2016, 107 p.
103. **Artur Tamm.** High entropy alloys: study of structural properties and irradiation response. Tartu, 2016, 115 p.
104. **Rasmus Talviste.** Atmospheric-pressure He plasma jet: effect of dielectric tube diameter. Tartu, 2016, 107 p.
105. **Andres Tiko.** Measurement of single top quark properties with the CMS detector. Tartu, 2016, 161 p.
106. **Aire Olesk.** Hemiboreal Forest Mapping with Interferometric Synthetic Aperture Radar. Tartu, 2016, 121 p.
107. **Fred Valk.** Nitrogen emission spectrum as a measure of electric field strength in low-temperature gas discharges. Tartu, 2016, 149 p.
108. **Manoop Chenchiliyan.** Nano-structural Constraints for the Picosecond Excitation Energy Migration and Trapping in Photosynthetic Membranes of Bacteria. Tartu, 2016, 115p.
109. **Lauri Kaldamäe.** Fermion mass and spin polarisation effects in top quark pair production and the decay of the higgs boson. Tartu, 2017, 104 p.
110. **Marek Oja.** Investigation of nano-size α- and transition alumina by means of VUV and cathodoluminescence spectroscopy. Tartu, 2017, 89 p.
111. **Viktoriia Levushkina.** Energy transfer processes in the solid solutions of complex oxides. Tartu, 2017, 101 p.
112. **Mikk Antsov.** Tribomechanical properties of individual 1D nanostructures: experimental measurements supported by finite element method simulations. Tartu, 2017, 101 p.

113. **Hardi Veermäe.** Dark matter with long range vector-mediated interactions. Tartu, 2017, 137 p.

114. **Aris Auzans.** Development of computational model for nuclear energy systems analysis: natural resources optimisation and radiological impact minimization. Tartu, 2018, 138 p.

115. **Aleksandr Gurev**. Coherent fluctuating nephelometry application in laboratory practice. Tartu, 2018, 150 p.

116. **Ardi Loot**. Enhanced spontaneous parametric downconversion in plasmonic and dielectric structures. Tartu, 2018, 164 p.

117. **Andreas Valdmann.** Generation and characterization of accelerating light pulses. Tartu, 2019, 85 p.

118. **Mikk Vahtrus.** Structure-dependent mechanical properties of individual one-dimensional metal-oxide nanostructures. Tartu, 2019, 110 p.

119. **Ott Vilson.** Transformation properties and invariants in scalar-tensor theories of gravity. Tartu, 2019, 183 p.

120. **Indrek Sünter.** Design and characterisation of subsystems and software for ESTCube-1 nanosatellite. Tartu, 2019, 195 p.

121. **Marko Eltermann**. Analysis of samarium doped $TiO_2$ optical and multi-response oxygen sensing capabilities. Tartu, 2019, 113 p.

122. **Kalev Erme**. The effect of catalysts in plasma oxidation of nitrogen oxides. Tartu, 2019, 114 p.

123. **Sergey Koshkarev.** A phenomenological feasibility study of the possible impact of the intrinsic heavy quark (charm) mechanism on the production of doubly heavy mesons and baryons. Tartu, 2020, 134 p.